Mon. Not. R. Astron. Soc. **353,** 953–979 (2004) doi:10.1111/j.1365-2966.2004.08140.x

A deep survey of heavy element lines in planetary nebulae – II. Recombination-line abundances and evidence for cold plasma

Y. G. Tsamis,[1,2]★ M. J. Barlow,[1] X.-W. Liu,[1]† P. J. Storey[1] and I. J. Danziger[3]

[1]*Department of Physics and Astronomy, University College London, Gower Street, London WC1E 6BT*

[2]*LUTH, Laboratoire l'Univers et ses Théories, associé au CNRS (FRE 2462) et á l'Université Paris 7, Observatoire de Paris-Meudon, F-92195 Meudon Cédex, France*

[3]*Osservatorio Astronomico di Trieste, Via G. B. Tiepolo 11, I-34131 Trieste, Italy*

Accepted 2004 June 16. Received 2004 June 15; in original form 2004 April 7

ABSTRACT

In our Paper I, we presented deep optical observations of the spectra of 12 Galactic planetary nebulae (PNe) and three Magellanic Cloud PNe, carrying out an abundance analysis using the collisionally excited forbidden lines. Here, we analyse the relative intensities of faint optical recombination lines (ORLs) from ions of carbon, nitrogen and oxygen in order to derive the abundances of these ions relative to hydrogen. The relative intensities of four high-*l* C II recombination lines with respect to the well-known 3d–4f λ4267 line are found to be in excellent agreement with the predictions of recombination theory, removing uncertainties about whether the high C^{2+} abundances derived from the λ4267 line could be due to non-recombination enhancements of its intensity.

We define an abundance discrepancy factor (ADF) as the ratio of the abundance derived for a heavy element ion from its recombination lines to that derived for the same ion from its ultraviolet, optical or infrared collisionally excited lines (CELs). All of the PNe in our sample are found to have ADFs that exceed unity. Two of the PNe, NGC 2022 and LMC N66, have O^{2+} ADFs of 16 and 11, respectively, while the remaining 13 PNe have a mean O^{2+} ADF of 2.6, with the smallest value being 1.8.

Garnett and Dinerstein found that for a sample of about 12 PNe the magnitude of the O^{2+} ADF was inversely correlated with the nebular Balmer line surface brightness. We have investigated this for a larger sample of 20 PNe, finding weak correlations with decreasing surface brightness for the ADFs of O^{2+} and C^{2+}. The C^{2+} ADFs are well correlated with the absolute radii of the nebulae, although no correlation is present for the O^{2+} ADFs. We also find both the C^{2+} and O^{2+} ADFs to be strongly correlated with the magnitude of the difference between the nebular [O III] and Balmer jump electron temperatures (ΔT), corroborating a result of Liu et al. for the O^{2+} ADF. ΔT is found to be weakly correlated with decreasing nebular surface brightness and increasing absolute nebular radius.

There is no dependence of the magnitude of the ADF upon the excitation energy of the ultraviolet, optical or infrared CEL transition used, indicating that classical nebular temperature fluctuations – i.e. in a chemically homogeneous medium – are not the cause of the observed abundance discrepancies. Instead, we conclude that the main cause of the discrepancy is enhanced ORL emission from cold ionized gas located in hydrogen-deficient clumps inside the main body of the nebulae, as first postulated by Liu et al. for the high-ADF PN, NGC 6153. We have developed a new electron temperature diagnostic, based upon the relative intensities of the O II 4f–3d λ4089 and 3p–3s λ4649 recombination transitions. For six out of eight PNe for which both transitions are detected, we derive O^{2+} ORL electron temperatures of $\leqslant$300 K, very much less than the O^{2+} forbidden-line and H^{+} Balmer jump temperatures derived for the same nebulae. These results provide direct observational evidence for the presence of cold

★E-mail: yiannis.tsamis@obspm.fr

†Current address: Department of Astronomy, Peking University, Beijing, China.

plasma regions within the nebulae, consistent with gas cooled largely by infrared fine-structure transitions; at such low temperatures, recombination transition intensities will be significantly enhanced due to their inverse power-law temperature dependence, while ultraviolet and optical CELs will be significantly suppressed.

Key words: ISM: abundances – planetary nebulae: general.

1 INTRODUCTION

This is the second of two papers devoted to the study of elemental abundances in a sample of Galactic and Magellanic Cloud planetary nebulae (PNe). In a companion paper (Tsamis et al. 2003a), we have presented a similar analysis of a number of Galactic and Magellanic Cloud H II regions. The main focus of these papers is on the problem of the optical recombination-line (ORL) emission from heavy element ions (e.g. C^{2+}, N^{2+}, O^{2+}) in photoionized nebulae. The main manifestation of this problem is the observed discrepancy between nebular elemental abundances derived from weak ORLs (such as C II λ4267, N II λ4041, O II λλ4089, 4650) on the one hand and the much brighter collisionally-excited lines (CELs; often collectively referred to as forbidden lines) on the other (Kaler 1981; Peimbert, Storey & Torres-Peimbert 1993; Liu et al. 1995, hereafter LSBC; Liu et al. 2000, 2001b; Garnett & Dinerstein 2001a; Tsamis 2002; Tsamis et al. 2003a), with ORLs typically being found to yield ionic abundances that are factors of 2 or more larger than those obtained from CELs emitted by the same ions. A closely linked problem involves the observed disparity between the nebular electron temperatures derived from the traditional [O III] (λ4959+λ5007)/λ4363 CEL ratio and the H I Balmer discontinuity diagnostic: the latter yields temperatures that are in most cases lower than those derived from the [O III] ratio (Peimbert 1971; Liu & Danziger 1993b, hereafter LD93b; Liu et al. 2001b; Tsamis 2002).

The ORL analysis of the current paper is based upon deep optical spectra of 12 Galactic and three Magellanic Cloud PNe that we have acquired (Tsamis et al. 2003b, hereafter Paper I). In Paper I we described how the observations were obtained and reduced and presented tabulations of observed and dereddened relative intensities for the detected lines. CELs in the spectra were used to derive nebular electron temperatures and densities from a variety of diagnostic ratios. CEL-based abundances were also derived for a range of heavy elements, using standard ionization correction factor (*icf*) techniques to correct for unobserved ion stages.

In the current paper, we analyse the ORL data that were presented in Paper I. In Section 2 we derive recombination-line ionic abundances for a number of carbon, nitrogen and oxygen ions. In Section 3 we present a comparison between total C, N and O abundances derived from ORLs and from ultraviolet (UV), optical and infrared (IR) CELs and we derive abundance discrepancy factors (ADFs; the ratio of the abundances derived for the same ion from ORLs and from CELs) for a range of carbon, nitrogen and oxygen ions. In Section 4 we investigate how ORL/CEL ADFs correlate with other nebular parameters, such as the difference between [O III] forbidden-line and H I Balmer jump (BJ) temperatures, the Hβ nebular surface brightness and the nebular absolute radius. In Section 5 we look at whether the observational evidence provides support for the presence of classical Peimbert-type temperature fluctuations within the nebulae, and whether the observational evidence points to strong density variations within the nebulae. In Section 6 we present evidence for the presence of cold plasma ($T_e \leqslant 2000$ K) in a number of nebulae in our sample, making use of the fact that the strengths of several well-observed O II and He I recombination lines have sufficiently different temperature dependences for the relative intensities of two O II lines, or two He I lines, to be used as diagnostics of the electron temperatures prevailing in their emitting regions. In Section 7 we summarize our conclusions.

2 RECOMBINATION-LINE ABUNDANCES

2.1 Carbon ions: C^{2+}/H^+, C^{3+}/H^+ and C^{4+}/H^+

We have detected recombination lines of carbon from all of the PNe, with the exception of LMC N66. C II lines, in particular, were detected from all galactic nebulae, as well as from SMC N87 and LMC N141; C III lines were detected from the majority of them, excluding NGC 3132 and My Cn 18 only. The strongest observed C II ORL is the λ4267 (V6) 3d–4f transition, which was consistently recorded with a high signal-to-noise (S/N) ratio in our high-resolution deep spectra (see fig. 1 in Paper I). We derived C^{2+}/H^+ abundance ratios from it using the effective recombination coefficients of Davey, Storey & Kisielius (2000), which include both radiative and dielectronic processes; it should be noted that abundance ratios derived using the λ4267 line are insensitive to the adoption of Case A or B. The C II λ4267 line has been used in the past in abundance analyses of galactic PNe (e.g. Kaler 1986; Rola & Stasińska 1994) with conflicting results. It has also been detected from a number of Large Magellanic Cloud (LMC) and Small Magellanic Cloud (SMC) PNe (Barlow 1987; Meatheringham & Dopita 1991; and from SMC N42 by Vassiliadis et al. 1992). No detections of this line have been reported, however, for LMC N141 and SMC N87 and carbon ORLs have not been used to date in abundance studies of Magellanic Cloud PNe.

Because of the structure of the C^+ ion, the configuration of the valence orbital gives rise to only one atomic term, compared to three atomic terms for N^+ and O^+ (e.g. Kuhn 1969; Allen 1973). As a result, there are fewer C II recombination lines than of O II or N II, so they are of greater intensity. As an observational consequence of this fact, in several PNe of our sample we have also detected C II recombination lines from higher principal quantum numbers, originating from states above the 4f $^2F^o$ level. In Table 1 we compare the observed intensities of these lines of high excitation energy, normalized such that $I(\lambda4267) = 1.00$, against the recombination theory predictions of Davey et al. (2000). This permits us to check whether the 4f $^2F^o$–ng ^2G transitions which populate the upper level of 3d–4f λ4267 can be safely attributed to recombination only, or whether unidentified processes contribute as well. This is of importance in the light of results from this and previous works – e.g. the PN studies of Kaler (1981, 1986), Rola & Stasińska (1994), LSBC, Liu et al. (2000) as well as the H II region analysis of Tsamis et al. (2003a) – which found that the C^{2+}/H^+ abundances derived from the λ4267 recombination line are often significantly higher than those derived from the collisionally excited C III] λ1908 line. This

Table 1. High-excitation C II recombination-line relative intensities. In column 6, the value before the dash is for the entire nebula and the value after is from a fixed-slit observation.

λ_0 (Å)	Trans.	NGC 3242 I_{obs}	NGC 5315 I_{obs}	NGC 5882 I_{obs}	IC 4191 I_{obs}	Orion(M42) I_{obs}	Theory I_{pred}
4267.15	3d–4f	1.000	1.000	1.000	1.000	1.000	1.000
6151.43	4d–6f	0.030	–	–	–|0.055	0.038	0.040
6461.95	4f–6g	0.102	0.095	0.153	0.166|0.144	0.087	0.103
5342.38	4f–7g	0.065	–	–	–|0.056	0.049	0.053
4802.23	4f–8g	0.031	0.020	0.025	–	0.034	0.031

fact had sometimes been attributed in the past to erroneous recombination coefficients, inaccurate line detections, or blending of the λ4267 transition with a line from an unknown ionic species.

In the case of NGC 3242, Table 1 shows that the agreement between observations and theory is excellent for all detected lines. The $4f\,^2F^o$–$7g\,^2G$ λ5342 line is blended with a feature identified as [Kr IV] λ5345.9 (cf. Hyung, Aller & Feibelman 1999, their table 6) and its intensity was retrieved through Gaussian profile fitting. For NGC 5315, the agreement is very good for both detected lines of high excitation. For NGC 5882, the λ6462 line is stronger by 49 per cent and the λ4802 line weaker by 19 per cent than predicted, relative to λ4267. For IC 4191, as measured on the fixed-slit spectrum, the former line is stronger than predicted by 40 per cent, while the λ5342 line is within 8 per cent of the predicted value. It should be noted that, apart from λ4802, the other high-level C II lines are covered in our lower-resolution 4.5-Å FWHM spectra only and the modest discrepancies for NGC 5882 and IC 4191 regarding the λ6462 line are within the estimated error margins. In the above cases, the λ4802 line was deblended from the N II λ4803.3 line via Gaussian line fitting.

In conclusion, the good consistency among the observed and predicted relative intensities of C II $4f\,^2F^o$–$ng\,^2G$ transitions in this PN sample suggests that there is no other mechanism competing with recombination that could contribute to the excitation of the 3d–4f λ4267 line. Thus, the high S/N ratio detections of the other C II lines from the current PN sample indicate that C II λ4267 is a reliable C^{2+} abundance diagnostic. A similar conclusion can be drawn from the C II recombination lines found in the spectrum of the Orion nebula (M42). In Table 1 we extend the above comparison to 4f–*n*g C II transitions from M42, whose intensities were presented by Baldwin et al. (2000). These authors did not mark the listed lines as C II transitions, but left them unidentified (see their table 1). However, the measured wavelengths and our examination of their relative intensities leave no doubt as to their identity. The agreement with theory is excellent in this case as well, confirming beyond reasonable doubt the interpretation of recombination excitation for these lines.

The C^{3+}/H^+ abundance ratios were derived from the λ4187 (V18) line and from the λ4650 (V1) multiplet, using the effective radiative and dielectronic recombination coefficients of Péquignot, Petitjean & Boisson (1991) and Nussbaumer & Storey (1984), respectively; they are insensitive to the assumption of Case A or B. The C III (V16) triplet at λ4069 was also detected from NGC 2022, 3242, 5882 and 6818. This multiplet is primarily excited by radiative recombination and is usually seriously blended with [S II] and O II V10 lines in medium resolution spectra; its overall intensity was retrieved via multiple Gaussian fitting. As was noted by Liu (1998), the observed relative intensities of C III V16, V18 and V1 multiplets are not in accord with theoretical predictions; in an analysis of the spectrum of NGC 4361 he found that the C^{3+}/H^+ abundance ratio derived from these three C III multiplets spans a range of 0.4 dex, which he attributed to probable uncertainties in the effective recombination coefficients. The four PNe for which all V16, V18 and V1 multiplets have been detected offer a further testing ground for the reliability of current ORL C III recombination coefficients. An instructive case is that of the high-excitation nebula, NGC 2022. As is apparent from our high-resolution 1.5-Å FWHM spectra of this object, the auroral [S II] λλ4068, 4075 lines are virtually absent and the observed intensity of C III V16 is most accurately recorded, because it is less affected by blending effects. In this nebula, the observed C III λλ4069, 4187 and λ4650 multiplets have intensity ratios of 1.80 : 0.34 : 1.00, versus the theoretical ratios of 0.59 : 0.21 : 1.00 calculated using the effective radiative and dielectronic recombination coefficients of Péquignot et al. (1991) and Nussbaumer & Storey (1984), respectively. In the case of NGC 5882, the observed multiplet intensities show ratios of 2.38 : 0.22 : 1.00. Similarly for IC 4191, where C III λ4069 is not detected, the observed intensities of λ4187 (V18) and λ4650 (V1) have a ratio of 0.20 : 1.00. We see that the theoretical predictions for the relative intensities of λ4187 and λ4650 appear to be more secure than that for λ4069. It would seem that the effective recombination coefficient for the λ4069 V16 multiplet has been underestimated by a factor of ∼2–4, or else that it is blended with an unknown line from an ion of similar excitation.

As a result of the above discussion, in our ORL abundance analysis for C^{3+} we have discarded values derived from the λ4069 triplet. Instead, we have adopted C^{3+}/H^+ abundance ratios as derived from an intensity-weighted mean of the C III λ4187 and λ4650 lines.

Regarding C^{4+}, we have derived C^{4+}/H^+ fractions for a number of Galactic PNe from the C IV λ4658 line, using the Case A effective recombination coefficients of Péquignot et al. (1991). The ionic and total carbon abundances derived from recombination lines are presented in Tables 2 and 3 for the Galactic and Magellanic Cloud PNe, respectively (see Appendix A for a discussion of the adopted *icf* scheme in the derivation of total C abundances).

2.2 Nitrogen ions: N^{2+}/H^+, N^{3+}/H^+ and N^{4+}/H^+

We have detected recombination lines from all Galactic PNe and from up to three ionization stages of nitrogen. Nitrogen ORLs were not detected from any of the three Cloud nebulae. Both 3s–3p as well as 3d–4f transitions were recorded. The derived recombination-line N^{2+}, N^{3+}, N^{4+} and total N abundances are presented in Tables 4 and 5 (see also Appendix A).

The N^{2+}/H^+ fractions were derived using effective recombination coefficients from Escalante & Victor (1990), assuming Case A for singlets and Case B for triplets. The adopted N^{2+}/H^+ abundances are derived for each nebula by averaging the values obtained from each N II line, weighted according to the predicted relative intensity of the transition. The λ4379 (V18) N III recombination line was

Table 2. Recombination-line carbon abundances for Galactic PNe.

	NGC 3242	**NGC 5882**	**NGC 5315**	**NGC 3918**	**NGC 2022**	**NGC 6818**
$I(\lambda4267)$	0.620	0.399	0.706	0.497	0.820	0.449
$10^4 \times C^{2+}/H^+$	6.15	3.77	6.60	5.02	8.83	4.69
$I(\lambda4069)$	0.755	0.412	–	–	1.75	0.957
$10^4 \times C^{3+}/H^+$	3.64	2.11	–	–	7.49	3.97
$I(\lambda4187)$	0.204	0.0376	0.0107	0.152	0.332	0.118
$10^4 \times C^{3+}/H^+$	2.83	0.552	0.161	2.03	4.07	1.41
$I(\lambda4650)$	0.590	0.173	–	0.418	0.974	0.389
$10^4 \times C^{3+}/H^+$	1.75	0.522	–	1.22	2.77	1.10
Adopted						
$10^4 \times C^{3+}/H^+$	2.03	0.527	0.161	1.44	3.10	1.37
$I(\lambda4658)$	0.0776	–	–	0.109	1.03	0.180
$10^4 \times C^{4+}/H^+$	0.188	–	–	0.262	2.62	0.447
icf(C)	1.010	1.030	1.078	1.116	1.020	1.185
$\mathbf{10^4 \times C/H}$	**8.45**	**4.43**	**7.29**	**7.50**	**14.84**	**7.71**
	NGC 3132	**NGC 2440**	**NGC 6302**	**IC 4406**	**IC 4191**	**My Cn 18**
$I(\lambda4267)$	0.697	0.403	0.163	0.805	0.546	0.252
$10^4 \times C^{2+}/H^+$	6.60	4.47	2.00	7.72	5.16	3.80
$I(\lambda4187)$	–	0.222	–	0.0912	0.0711	–
$10^4 \times C^{3+}/H^+$	–	2.58	–	1.32	1.04	–
$I(\lambda4650)$	–	0.337	0.0754[a]	0.238	0.359	–
$10^4 \times C^{3+}/H^+$	–	1.06	–	0.715	1.08	–
Adopted						
$10^4 \times C^{3+}/H^+$	–	1.66	–	0.883	1.07	–
$I(\lambda4658)$	–	0.722	–	–	–	–
$10^4 \times C^{4+}/H^+$	–	1.82	–	–	–	–
icf(C)	1.930	1.284	2.725	1.310	1.040	1.589
$\mathbf{10^4 \times C/H}$	**12.74**	**10.21**	**5.45**	**11.27**	**6.48**	**6.04**

[a]From C III λ4647.

detected from all Galactic PNe, except NGC 5315 and My Cn 18. We derived N^{3+}/H^+ abundances from it using the effective radiative and dielectronic recombination coefficients of Péquignot et al. (1991) and Nussbaumer & Storey (1984) respectively. The N IV 5g–6h λ4606 line has also been detected from the high-excitation nebulae NGC 2022, 2440, 3918, 6302 and 6818; it was used for the derivation of N^{4+}/H^+ abundances employing effective recombination coefficients as in the case of N III λ4379.

2.3 Oxygen ions: O^{2+}/H^+, O^{3+}/H^+ and O^{4+}/H^+

Our observations provide us with one of the most extensive records of O II recombination spectra in gaseous nebulae thus far, obtained for PNe possessing a wide range of physical conditions. For the first time also to our knowledge, O II lines have been detected and measured from Magellanic Cloud PNe (SMC N87, LMC N66 and LMC N141). This allowed us to obtain accurate ORL O^{2+}/H^+ abundances for all our nebulae and permitted a comprehensive investigation of the occurrence of the discrepancy between recombination-line O^{2+} abundances and those derived in the usual manner from forbidden lines of O^{2+}. Furthermore, having such an extensive inventory of O II line intensities, we are able to perform a thorough comparison with current theoretical predictions of the O II recombination spectrum (see Appendix B).

In Table 6 we present ORL O^{2+}/H^+ ionic ratios for the complete sample (for the Magellanic Cloud objects, these ratios and total O abundances are listed in Table 3). Effective recombination coefficients are taken from Storey (1994) for 3s–3p transitions (under *LS*-coupling) and from LSBC for 3p–3d and 3d–4f transitions (under intermediate coupling), assuming Case A for doublet and Case B for quartet lines. For several nebulae, we have also detected lines arising from doubly excited spectral terms, such as multiplet V15 $3s'\,^2D$–$3p'\,^2F^o$ at 4590 Å (see Paper I). The excitation of this multiplet is dominated by dielectronic recombination, but we have not derived abundance ratios from it because the existing recombination coefficients are not of the desired accuracy.[1] For each PN, the mean O^{2+}/H^+ fractions derived by averaging the values from all 3–3 multiplets and the co-added 3d–4f transitions have been adopted as the recombination-line values in the subsequent discussion. The O^{2+}/H^+ values listed for the 3d–4f lines in Table 6 were obtained by summing all the intensities and dividing by the sum of all the recombination coefficients, allowing for weak unobserved or blended multiplet components, as listed in table 4(a) of LSBC.

In Table 7 we present a summary of the oxygen recombination-line ionic and total abundances, including the O^{3+}/H^+ fractions for several PNe derived by Liu & Danziger (1993a) from the O III V8

[1] Garnett & Dinerstein (2001a) noted that, for a sample of about 12 PNe, O^{2+} abundances derived from multiplet V15 of O II were anomalously high compared to those derived from other O II multiplets, owing either to an underestimated dielectronic recombination coefficient for this multiplet, or to additional contributions, e.g. high-temperature dielectronic recombination originating from very hot regions, which might also contribute to the strengths of other O II lines. Liu et al. (2001b) looked at this issue in detail and concluded that the discrepancy was most likely due to the lower accuracy of the recombination coefficients available for the V15 multiplet.

Table 3. Carbon and oxygen recombination-line abundances for Magellanic Cloud PNe.

	SMC N87	LMC N66	LMC N141
$I(\lambda 4267)$	0.672	–	0.683
$10^4 \times C^{2+}/H^+$	6.73	–	6.79
$I(\lambda 4187)$	0.108	–	0.0522
$10^4 \times C^{3+}/H^+$	1.46	–	0.733
$I(\lambda 4650)$	0.141	–	0.181
$10^4 \times C^{3+}/H^+$	0.413	–	0.538
Adopted			
$10^5 \times C^{3+}/H^+$	6.75	–	5.82
$I(\lambda 4658)$	–	–	–
$10^4 \times C^{4+}/H^+$	–	–	–
icf(C)	1.020	–	1.023
$10^4 \times$ C/H	**7.55**	**–**	**7.54**
$I(\lambda 4069) \mid O^{2+}$	–	–	0.188|7.27
$I(\lambda 4072) \mid O^{2+}$	–	–	0.124|5.15
$I(\lambda 4075) \mid O^{2+}$	–	–	0.254|7.30
$I(\lambda 4638) \mid O^{2+}$	0.0832|7.73	–	0.0255|2.38
$I(\lambda 4641) \mid O^{2+}$	0.0831|3.06	–	0.120|4.45
$I(\lambda 4649) \mid O^{2+}$	0.0781|1.51	0.227|3.98	0.127|2.47
$I(\lambda 4650) \mid O^{2+}$	0.0781|7.26	0.227|19.1	0.0836|7.81
$I(\lambda 4661) \mid O^{2+}$	0.0243|1.76	–	0.0518|3.79
$I(\lambda 4676) \mid O^{2+}$	0.0248|2.15	–	0.0465|4.04
Adopted			
$10^4 \times O^{2+}/H^+$	2.95	8.53	4.96
CEL O^+/O^{2+}	0.018	0.076	0.023
icf(O)	1.000	3.770	1.000
$10^4 \times$ O/H	**3.00**	**34.6**	**5.08**

multiplet at 3265 Å; we also list O^{4+}/H^+ fractions derived from the O IV λ4632 line which was detected from the high-excitation nebulae NGC 3918, 2022, 6818, 2440 and 6302. For the latter calculation, we used the Case A dielectronic recombination coefficients of Nussbaumer & Storey (1984) and the radiative recombination coefficients of Péquignot et al. (1991). For a discussion on the derivation of total O abundances, the reader is referred to Appendix A.

3 COMPARISON OF ORL AND CEL ABUNDANCES

3.1 Total C, N and O abundances

The total elemental abundances of C, N and O obtained for the current PN sample from CELs (Paper I) and from ORLs are presented in Table 8, on the usual log N(H) = 12.0 scale, where they are compared with average abundances for Galactic PNe (for both type I and non-type I nebulae) derived by Kingsburgh & Barlow (1994) and the solar photospheric abundances of Grevesse, Noels & Sauval (1996) and Allende Prieto, Lambert & Asplund (2001, 2002). Our method for the derivation of total elemental abundances from ORLs is discussed in detail in Appendix A.

3.2 Abundance grids and ionic ADFs

Comparisons between the ionic abundances obtained from the UV, optical and IR CELs (Paper I) and those from ORLs (Tables 2–7) are presented in Fig. 1 bringing together *International Ultraviolet Explorer* (*IUE*), optical, and *Infrared Space Observatory* (*ISO*) data for nine Galactic PNe, and *IUE* and optical data for the three Cloud PNe (LWS spectra are not available for NGC 2440 and My Cn 18, while *IUE* spectra are not available for IC 4191 and My Cn 18). Note that the plotted O^{2+}/H^+ fractions derived from optical CELs are those from the [O III] λλ4959, 5007 lines only.

In Paper I we used the *ISO* LWS far-IR fine-structure (FS) line fluxes presented by Liu et al. (2001a) to derive N^{2+}/H^+ and O^{2+}/H^+ abundances for eight PNe in our sample. In the meantime, we retrieved archived LWS spectra of NGC 2022 (TDT 69201604) and NGC 6818 (TDT 34301005) and measured the fluxes of the [N III] 57-μm and [O III] 52- and 88-μm FS lines. We scaled these to $I(\mathrm{H}\beta) = 100$ using the total nebular Hβ fluxes dereddened by the $c(\mathrm{H}\beta)^{\mathrm{radio}}$ constants of table 5 in Paper I. The respective I(52-μm), I(57-μm) and I(88-μm) intensities are 91.7, 21.5 and 42.2 for NGC 2022; and 164.6, 45.5 and 69.7 for NGC 6818. From the [O III] 52-μm/88-μm line ratio, we derived electron densities of 800 $\mathrm{cm^{-3}}$ for NGC 2022 and 950 $\mathrm{cm^{-3}}$ for NGC 6818. From the measured FS line intensities and adopting N_e from the [O III] FS line ratio, we derived $N^{2+}/H^+ = 2.75 \times 10^{-5}$ and $O^{2+}/H^+ = 1.07 \times 10^{-4}$ for NGC 2022; and 6.91×10^{-5} and 2.20×10^{-4}, respectively, for NGC 6818. On the other hand, adopting the mean of N_e from the [Cl III] and [Ar IV] optical line ratios (Paper I), we derived $N^{2+}/H^+ = 3.94 \times 10^{-5}$ and $O^{2+}/H^+ = 1.45 \times 10^{-4}$ for NGC 2022; and 1.15×10^{-4} and 3.41×10^{-4}, respectively, for NGC 6818. The latter values for these two PNe are plotted in Fig. 1.

Fig. 1 shows that in all nebulae, and for all ions where ionic abundances from both ORLs and CELs have been derived, the values from the ORLs are consistently higher than those derived from the CELs (UV, optical or IR). This includes the Magellanic Cloud nebulae SMC N87, LMC N66 and LMC N141; no such comparisons had been reported so far regarding extragalactic PNe. In Table 9 we present a listing of the ionic ADFs, ADF(X^{i+}), defined as the ratio of the ORL ionic abundance to the UV, optical (OPT) or IR CEL ionic abundance. For comparison, data for the previously studied PNe NGC 7009 (LSBC), NGC 6153 (Liu et al. 2000), the Galactic bulge nebulae M1-42, M2-36 (Liu et al. 2001b), as well as for NGC 6644 and 6572 – from unpublished European Southern Observatory (ESO) 1.52-m observations – are also included.

Possible exceptions to the general pattern of large ADF(X^{i+}) values include C^{3+}/H^+ in NGC 3918, where abundances derived from the C III λλ4187, 4650 ORLs and the C IV λ1550 resonant doublet almost coincide. For the same nebula, the N^{4+}/H^+ abundance obtained from the N IV λ4606 ORL is 10 per cent less than the value derived from the N V λ1240 CEL; also N^{3+}/H^+ in NGC 6302, where identical values are derived from the N III λ4379 ORL and the N IV] λ1486 intercombination line. This could be due to an underestimation on our part of the actual electron temperature pertaining to highly ionized species in these two high-excitation nebulae. Adopting a higher T_e in order to derive C^{3+}/H^+, N^{3+}/H^+ and N^{4+}/H^+ would result in lower CEL abundances and produce a discrepancy with the ORL values as well. Alternatively, it could mean that at least in some nebulae the mechanisms that are responsible for the abundance discrepancies do not affect species of different ionization degree in the same way.

The current work has revealed two further nebulae, NGC 2022 and LMC N66, which exhibit extreme ORL/CEL ADFs: factors of 16 and 11, respectively, for O^{2+}/H^+. These nebulae are added to a rare class of PNe, along with NGC 6153, M1-42, and Hf 2-2, that exhibit ORL/CEL ADFs of 10 or more. We also reveal another object, the type I bipolar nebula NGC 2440, whose ORL/CEL ADF of 5 is similar to those of NGC 7009 and M2-36 (see Table 9).

Taking into account that in Paper I we presented both 'low-density' values (adopting [O III] 88-μm/52-μm densities) and

Table 4. Recombination-line N^{2+}/H^{+} abundances for Galactic PNe.

λ_0 (Å)	Mult.	I_{obs}	N^{2+}/H^{+} (10^{-4})	I_{obs}	N^{2+}/H^{+} (10^{-4})	I_{obs}	N^{2+}/H^{+} (10^{-4})	I_{obs}	N^{2+}/H^{+} (10^{-4})
		NGC 3242		**NGC 5882**		**NGC 5315**		**NGC 3918**	
V3 3s $^3P^o$–3p ^3D									
5666.63	V3	0.0321	2.34	–	–	–	–	–	–
5676.02	V3	0.0134	2.20	0.0189	3.10	–	–	–	–
5679.56	V3	0.0428	1.68	0.0604	2.36	–	–	–	–
V5 3s $^3P^o$–3p ^3P									
4601.48	V5	0.0050	1.19	–	–	–	–	–	–
4607.16	V5	–	–	–	–	–	–	–	–
4621.39	V5	–	–	–	–	–	–	–	–
4630.54	V5	0.0179	1.43	–	–	–	–	–	–
3d–4f									
4041.31	V39b	0.0128	0.88	0.0273	1.79	0.0573	3.71	0.0134	0.94
4237.05	V48b	0.0173	1.71	0.0139	1.38	0.0166	1.64	0.0163	1.65
4241.78	V48a	–	–	–	–	0.0422	4.16	0.0163	1.75
4530.41	V58b	–	–	0.0180	1.75	–	–	0.0148	1.55
4678.14	V61b	–	–	–	–	0.0312	4.80	–	–
Sum		**0.141**	**1.71**	**0.138**	**2.24**	**0.147**	**3.43**	**0.0607**	**1.42**
		NGC 6302		**IC 4191**		**NGC 6818**		**NGC 2022**	
V3 3s $^3P^o$–3p ^3D									
5666.63	V3	–	–	0.0921	6.90	–	–	–	–
5676.02	V3	–	–	0.0400	6.58	0.0322	5.29	0.0288	4.73
5679.56	V3	–	–	0.1282	5.02	0.1029	4.03	0.0921	3.61
V5 3s $^3P^o$–3p ^3P									
4630.54	V5	0.0743	5.55	0.0549	4.50	–	–	–	–
V28 3s $^3P^o$–3p $^3D^o$									
5927.81	V28	0.0205	8.26	–	–	–	–	–	–
5931.78	V28	0.0361	6.47	0.0460	5.73	–	–	–	–
3d–4f									
4041.31	V39b	–	–	0.0639	4.26	–	–	0.0580	4.27
Sum		**0.131**	**5.64**	**0.425**	**5.50**	**0.135**	**4.27**	**0.179**	**4.38**
		NGC 3132		**NGC 2440**		**IC 4406**		**My Cn 18**	
V3 3s $^3P^o$–3p ^3D									
5676.02	V3	0.0249	4.10	–	–	–	–	–	–
5679.56	V3	0.0799	3.13	–	–	–	–	–	–
V5 3s $^3P^o$ –3p ^3P									
4607.16	V5	–	–	–	–	–	–	0.0842	26.7
4621.39	V5	–	–	–	–	–	–	0.0731	23.3
4630.54	V5	0.0411	3.40	–	–	0.2318	1.90	0.2099	17.9
3d–4f									
4041.31	V39b	–	–	0.0618	4.28	–	–	–	–
4237.05	V48b	–	–	0.0495	4.90	–	–	–	–
4241.78	V48a	–	–	0.0558	5.89	–	–	–	–
4530.41	V58b	–	–	0.0415	4.28	–	–	–	–
Sum		**0.146**	**3.40**	**0.209**	**4.77**	**0.232**	**1.90**	**0.283**	**20.4**

'high-density' values (adopting densities from [Ar IV], [Cl III]), we note the following regarding the N^{2+}/H^{+} and O^{2+}/H^{+} fractions derived from the far-IR FS lines that were plotted in Fig. 1. For NGC 3132 and IC 4406, which have a low mean density, the 'low-density' values are plotted for both N^{2+} and O^{2+}, while for all remaining PNe (including NGC 2022 and 6818), which are of higher mean densities, the 'high-density' values are plotted. From our Paper I discussion of the results of Rubin (1989) it follows that the low critical densities of the far-IR N^{2+} and O^{2+} lines lead to their emission being biased towards lower-than-average density nebular regions. This is not true for the UV and optical lines, whose emissivity ratios relative to Hβ are less sensitive to variations in nebular density, owing to the significantly higher critical densities of the lines in question. However, it is obvious from Fig. 1 and Table 9 that the N^{2+} and O^{2+} abundances deduced from the IR FS lines agree very well with the values obtained from the N III] λ1750 and [O III] $\lambda\lambda$4959, 5007 lines. This shows that, even though density variations are present in the nebulae, no significant bias in the inferred CEL abundances is present, because very satisfactory agreement amongst the derived values is achieved (see also the relevant discussion in Section 5.1). Alternatively, this could mean that whatever other bias there is, it affects all UV, optical and IR CEL abundances in a rather similar manner.

In Sections 5.1 and 5.2 we will look further into the arguments for or against the existence of density or temperature fluctuations in our present PNe sample.

Table 5. Overall recombination-line nitrogen abundances for Galactic PNe.

	NGC 3242	**NGC 5882**	**NGC 5315**	**NGC 3918**	**NGC 2022**	**NGC 6818**
$10^4 \times N^{2+}/H^+$	1.71	2.24	3.43	1.42	4.38	4.27
$I(\lambda4379)$	0.158	0.136	–	0.146	0.472	0.203
$10^4 \times N^{3+}/H^+$	0.685	0.575	–	0.641	2.080	0.887
$I(\lambda4606)$	–	–	–	0.0660	0.112	0.0460
$10^4 \times N^{4+}/H^+$	–	–	–	0.207	0.368	0.146
CEL N^+/N^{2+}	0.008	0.028	0.163	0.203	0.013	0.241
$10^4 \times N/H$	**2.42**	**2.88**	**5.93**	**2.56**	**6.88**	**6.33**
	NGC 3132	**NGC 2440**	**NGC 6302**	**IC 4406**	**IC 4191**	**My Cn 18**
$10^4 \times N^{2+}/H^+$	3.40	4.77	5.64	1.90	5.00	20.35
$I(\lambda4379)$	0.0571	0.324	0.182	0.172	0.270	–
$10^4 \times N^{3+}/H^+$	0.247	1.430	0.807	0.731	1.150	–
$I(\lambda4606)$	–	0.475	0.668	–	–	–
$10^4 \times N^{4+}/H^+$	–	1.70	2.28	–	–	–
CEL N^+/N^{2+}	1.296	0.475	0.435	0.536	0.393	–
$10^4 \times N/H$	**8.05**	**10.17**	**11.18**	**3.65**	**8.12**	**⩾20.35**

3.3 C/O and N/O elemental ratios

Tables 10 and 11 respectively present the (C^{2+}/O^{2+}, C/O) and (N^{2+}/O^{2+}, N/O) abundance ratios derived from pure ORL and pure CEL line ratios. In both tables, the last column may contain two values: the one before the vertical line is computed with the total oxygen CEL abundance found if we use the $O^{2+}(\lambda4959 + \lambda5007)/H^+$ ionic ratio in the *icf* method; the value after the vertical line adopts the oxygen abundance found using the $O^{2+}(\lambda1663)/H^+$ ratio. In the case of the CEL N/O ratio, the value after the vertical line is for nitrogen and oxygen CEL abundances computed by adopting the $N^{2+}(\lambda1751)/H^+$ and $O^{2+}(\lambda1663)/H^+$ ionic ratios, respectively, in the *icf* method.

The results presented in Tables 10 and 11 address an issue that we have noted in earlier papers: although CELs and ORLs can often yield very different abundances for the same ion relative to hydrogen, ORL-based and CEL-based abundance ratios for two different ions are usually quite comparable. This is because ORL/CEL ADFs are not very different from one ion to the next for a given nebula (Table 9). It appears that fairly reliable abundance ratios for ions (e.g. C^{2+}/O^{2+}) and for elements (e.g. C/O) may be obtained, provided that both abundances are based on the same type of line (e.g. ORL/ORL or CEL/CEL). It should be noted, however, that any residual differences between such ORL/ORL and CEL/CEL elemental ratios may be real and could yield clues about the relative nucleosynthetic histories of the ORL and CEL emitting media. Further study of this issue is encouraged. In Fig. 2 we show the CEL C^{2+}/O^{2+} and N^{2+}/O^{2+} ratios compared with the corresponding ratios derived from ORLs.

The criterion of Kingsburgh & Barlow (1994) states that type I PNe are those objects that have experienced envelope-burning conversion to nitrogen of dredged-up primary carbon, i.e. PNe with a N/O ratio greater than the (C + N)/O ratio of H II regions in the host galaxy, the latter being 0.8 for our own Galaxy. According to this criterion, three objects in our sample, NGC 2440, 6302 and My Cn 18, all bipolar, qualify as type I PNe by virtue of their ORL N/O ratios; however, only the first two qualify based on their CEL N/O ratios.

4 CORRELATIONS

4.1 ORL/CEL ADFs versus T_e discrepancies

The O^{2+} ORL/CEL ADF is known to be strongly correlated with the difference between the [O III] forbidden-line and H I BJ electron temperatures (Liu et al. 2001b). In Fig. 3 (top) we plot the ratio of C^{2+}/H^+ ionic abundances derived from the C II λ4267 ORL to those from the C III] λ1908 CEL versus the difference between the [O III] nebular to auroral forbidden-line temperature and the BJ temperature, for a sample of 17 PNe.

We see that a strong, positive linear correlation exists between

$$ADF(C^{2+}/H^+) \equiv \log(C^{2+}/H^+)_{ORL} - \log(C^{2+}/H^+)_{\lambda1908\,CEL},$$

and

$$\Delta T \equiv T_e([O\,III]) - T_e(BJ).$$

A linear fit to the 17 PNe plotted in Fig. 3 (top) yields

$$ADF\left(\frac{C^{2+}}{H^+}\right) = (0.419 \pm 0.051) + (14.6 \pm 1.8) \times 10^{-5}\Delta T, \quad (1)$$

with a linear correlation coefficient of 0.91.

The data include those for seven PNe from other studies: NGC 7009 (LSBC); NGC 4361 [Liu 1998; who quotes $C^{2+}(\lambda1908)/H^+$ values from Torres-Peimbert, Peimbert & Peña 1990]; NGC 6153 (Liu et al. 2000); M1-42 and M2-36 (Liu et al. 2001b); NGC 6644 (our unpublished observations); and NGC 2392 [ADF(C^{2+}) from Barker (1991); T_e(BJ) from LD93b]. The electron temperatures for the PNe in the current sample are taken from table 7 of Paper I.

Fig. 3 (bottom) shows that a very similar linear correlation also exists between $ADF(O^{2+}/H^+) \equiv \log(O^{2+}/H^+)_{ORL} - \log(O^{2+}/H^+)_{\lambda4959+5007\,CEL}$ and ΔT; see Liu et al. (2001b) for a

Table 6. Recombination-line O^{2+}/H^{+} abundances for galactic PNe.

λ_0 (Å)	Mult.	I_{obs}	O^{2+}/H^{+} (10^{-4})	I_{obs}	O^{2+}/H^{+} (10^{-4})
		NGC 3242		**NGC 5882**	
4638.86	V1	0.1692	15.9:	0.1690	16.2:
4641.81	V1	0.2152	8.00	0.2522	9.59
4649.13	V1	0.2231	4.36	0.3447	6.89
4650.84	V1	0.0979	9.18	0.1141	10.9
4661.63	V1	0.0870	6.38	0.1188	8.92
4673.73	V1	0.0304	13.1:	0.0188	9.10
4676.24	V1	0.0574	5.01	0.0906	8.10
V1 3s ^{4}P–3p ^{4}D^o		**0.681**	**6.02**	**0.939**	**8.29**
4317.14	V2	0.0454	5.39	0.0638	8.43
4319.63	V2	0.0227	2.74	0.0333	4.08
4325.76	V2	0.0311	20.3:	–	–
4345.56	V2	0.0881	11.1:	0.1100	14.6:
4349.43	V2	0.0712	3.71	0.0911	4.82
4366.89	V2	0.0909	10.6:	–	–
V2 3s ^{4}P–3p ^{4}P^o		**0.139**	**3.88**	**0.188**	**5.43**
4414.90	V5	0.0349	6.20	0.0439	8.51
4416.97	V5	0.0331	10.6	0.0399	13.9
4452.37	V5	0.0179	28.8:	–	–
V5 3s ^{2}P–3p ^{2}D^o		**0.068**	**7.77**	**0.084**	**10.4**
4069.89	V10	0.1828	7.08	0.1361	5.27
4072.16	V10	0.2153	8.95	0.2385	9.91
4075.86	V10	0.1664	4.79	0.2754	7.92
4078.84	V10	0.0213	5.81	–	–
4085.11	V10	0.0351	7.81	0.0290	6.45
4092.93	V10	0.0240	7.32	0.0212	6.45
V10 3p ^{4}D^o–3d ^{4}F		**0.645**	**6.71**	**0.700**	**7.58**
4121.46	V19	0.0283	9.81	0.0289	10.31
4129.32	V19	0.0517	79.2:	–	–
4132.80	V19	0.0210	3.87	0.0535	9.77
4153.30	V19	0.0304	3.91	0.0955	12.2
4156.53	V19	0.0373	30.1:	0.0728	58.3:
4169.22	V19	0.0126	4.76	0.0279	10.5
V19 3p ^{4}P^o–3d ^{4}P		**0.091**	**4.90**	**0.206**	**10.9**
4110.78	V20	–	–	0.0359	14.9
4119.22	V20	–	–	0.0919	10.3
V20 3p ^{4}P^o–3d ^{4}D		**–**	**–**	**0.128**	**11.3**
4890.86	V28	–	–	0.0086	7.39
4906.83	V28	–	–	0.0362	14.5
4924.53	V28	–	–	0.0656	15.4
V28 3p ^{4}P^o–3d ^{4}D		**–**	**–**	**0.110**	**13.9**
4083.90	V48b	0.0211	6.88	0.0210	6.58
4087.15	V48c	0.0204	7.04	0.0359	11.8
4089.29	V48a	0.1113	10.4	0.1452	12.9
4275.55	V67a	0.0310	4.47	0.0579	7.99
4276.75	V67b	0.0276	8.36	0.0236	7.65
4277.43	V67c	0.0172	6.90	0.0265	10.2
4282.96	V67c	0.0086	5.24	–	–
4283.73	V67c	0.0095	9.26	–	–
4285.69	V78b	0.0120	5.90	–	–
4288.82	V53c	0.0055	5.11	–	–
4291.25	V55	0.0162	9.27	0.0221	12.2
4292.21	V78c	0.0086	8.67	0.0078	7.56
4294.78	V53b	0.0314	10.2	0.0156	4.88
4303.83	V53a	0.0582	11.6	0.0573	10.9
4307.23	V53b	0.0087	7.71	–	–
4313.44	V78a	0.0086	6.59	–	–
4353.59	V76c	0.0098	8.98	0.0150	13.2
4357.25	V63a	0.0182	29.3:	–	–
4366.53	V75a	–	–	0.0605	7.13
4466.42	V86b	0.0260	23.7:	0.0305	26.7:
4477.90	V88	0.0145	15.7	–	–

Table 6 – *continued*

λ_0 (Å)	Mult.	I_{obs}	O^{2+}/H^{+} (10^{-4})	I_{obs}	O^{2+}/H^{+} (10^{-4})
		NGC 3242		**NGC 5882**	
4489.49	V86b	0.0055	7.86	–	–
4491.23	V86a	0.0235	16.0	0.0203	13.3
4609.44	V92a	0.0439	7.26	0.0609	9.64
4669.27	V89b	0.0119	27.6:	–	–
3d–4f		**0.493**	**8.40**	**0.569**	**9.67**
Adopted			**6.28**		**9.70**
		NGC 5315		**NGC 3918**	
4638.86	V1	0.1740	16.5:	0.2200	20.4:
4641.81	V1	0.2367	9.86	0.2168	7.96
4649.13	V1	0.3574	7.08	0.2108	4.07
4650.84	V1	0.0900	8.56	0.0415	3.84
4661.63	V1	0.0897	6.67	0.0743	5.39
4673.73	V1	0.0137	6.56	0.0310	14.5:
4676.24	V1	0.0789	6.99	0.0656	5.66
V1 3s ^{4}P–3p ^{4}D^o		**0.866**	**7.58**	**0.609**	**5.28**
4317.14	V2	0.0694	8.23	0.0417	4.93
4319.63	V2	0.0491	5.94	0.0170	2.04
4325.76	V2	0.0191	11.8:	0.0141	9.2:
4345.56	V2	0.0635	8.34	–	–
4349.43	V2	0.0744	9.77	0.0638	3.31
4366.89	V2	0.0589	6.87	–	–
V2 3s ^{4}P–3p ^{4}P^o		**0.315**	**6.06**	**0.123**	**3.39**
4414.90	V5	0.0721	13.0	0.0518	8.88
4416.97	V5	0.0620	20.2	0.0290	8.96
4452.37	V5	0.0146	29.8:	0.0653	100.:
V5 3s ^{2}P–3p ^{2}D^o		**0.134**	**15.55**	**0.081**	**8.91**
4069.62	V10	0.4263	16.5:	–	–
4072.16	V10	0.1879	7.78	–	–
4075.86	V10	0.1412	4.05	–	–
4085.11	V10	0.0437	9.69	–	–
V10 3p ^{4}D^o–3d ^{4}F		**0.329**	**5.58**	–	–
4121.46	V19	–	–	0.0920	33.1:
4132.80	V19	–	–	0.0180	3.32
4153.30	V19	–	–	0.0260	3.35
4156.53	V19	–	–	0.0370	29.9:
4169.22	V19	–	–	0.0045	1.72
V19 3p ^{4}P^o–3d ^{4}P		–	–	**0.049**	**3.07**
4083.90	V48b	0.0241	7.80	–	–
4087.15	V48c	0.0319	10.9	–	–
4089.29	V48a	0.0899	8.30	–	–
4275.55	V67a	0.1005	8.11	–	–
4303.82	V53a	0.0331	6.50	–	–
4609.44	V92a	0.0476	7.79	–	–
3d–4f		**0.332**	**8.08**	–	–
Adopted			**8.57**		**5.36**
		NGC 2022		**NGC 6818**	
4638.86	V1	0.1051	9.41:	0.2160	19.8:
4641.81	V1	0.2538	9.01:	0.4956	18.0:
4649.13	V1	0.3674	6.86	0.1687	3.23
4650.84	V1	0.0892	8.00	0.0262	2.50
4661.63	V1	0.1093	7.67	0.0851	6.11
4676.24	V1	0.0772	6.44	–	–
V1 3s ^{4}P–3p ^{4}D^o		**1.00**	**7.69**	**0.280**	**3.65**
4414.90	V5	0.1247	19.3	0.0594	9.90
V5 3s ^{2}P–3p ^{2}D^o		**0.125**	**19.3**	**0.059**	**9.90**
4069.78	V10	–	–	0.132	5.11
4072.16	V10	0.3164	13.1	0.175	7.26
4075.86	V10	0.2949	8.43	0.438	12.6
4085.11	V10	–	–	0.0722:	15.8:
V10 3p ^{4}D^o–3d ^{4}F		**0.611**	**10.3**	**0.745**	**6.41**

Table 6 – *continued*

λ_0 (Å)	Mult.	I_{obs}	O^{2+}/H^{+} (10^{-4})	I_{obs}	O^{2+}/H^{+} (10^{-4})
		NGC 2022		**NGC 6818**	
4089.29	V48a	0.2020	16.9	0.0984	9.37
4276.75	V67b	0.1856	13.8	–	–
4609.44	V92a	0.0578	10.0	–	–
3d–4f		**0.416**	**14.8**	**0.098**	**9.37**
Adopted			**13.0**		**7.33**
		NGC 3132		**IC 4406**	
4638.86	V1	0.1043	10.0	0.1817	17.3:
4641.81	V1	0.1706	6.49	0.2627	9.94
4649.13	V1	0.1649	3.30	0.2585	5.14
4650.84	V1	0.1226	11.8	0.0959	9.16
4661.63	V1	0.1157	8.70	0.0988	7.39
4676.24	V1	0.0762	6.82	0.0481	4.28
V1 3s ^{4}P–3p ^{4}D^o		**0.754**	**7.06**	**0.764**	**6.84**
4069.62	V10	0.4086	15.8:	0.4106	15.9:
4072.16	V10	0.1484	6.17	0.3776	15.7:
4075.86	V10	0.3592	10.3	0.2530	7.28
4085.11	V10	0.0433	9.64	–	–
V10 3p ^{4}D^o–3d ^{4}F		**0.551**	**8.70**	**0.253**	**7.28**
Adopted			**8.15**		**7.06**
		My Cn 18		**NGC 6302**	
4649.13	V1	0.2294	4.66	0.154	2.70
4650.84	V1	0.1531	14.9	0.0609	5.13
4661.63	V1	–	–	0.0353	2.33
Adopted			**6.43**		**3.28**
		IC 4191			
		Entire nebula		Fixed slit	
4638.86	V1	0.1912	18.0:	0.2426	22.8:
4641.81	V1	0.3218	12.0	0.2020	12.2
4649.13	V1	0.5439	10.7	0.5757	11.9
4650.84	V1	0.0997	9.38	0.1168	14.5
4661.63	V1	0.1539	11.3	0.1442	10.6
4676.24	V1	0.1226	10.8	0.1084	9.29
V1 3s ^{4}P–3p ^{4}D^o		**1.24**	**10.9**	**1.15**	**10.1**
4317.14	V2	–	–	0.0676	8.77
4319.63	V2	–	–	0.0551	6.62
4345.56	V2	–	–	0.1210	15.2
4349.43	V2	–	–	0.2324	12.1
4366.89	V2	–	–	0.1064	12.4
V2 3s ^{4}P–3p ^{4}P^o		**–**	**–**	**0.582**	**11.1**
4414.90	V5	0.0757	13.2	0.0546	9.49
4416.97	V5	0.0531	16.6	0.0444	13.9
V5 3s ^{2}P–3p ^{2}D^o		**0.129**	**14.4**	**0.099**	**11.1**
4069.62	V10	0.7056	27.2:	0.5998	23.2:
4072.16	V10	0.3654	15.2	0.3565	14.8
4075.86	V10	0.2883	8.28	0.3452	9.91
4085.11	V10	0.0503	11.0	0.0266	5.81
V10 3p ^{4}D^o–3d ^{4}F		**0.704**	**11.1**	**0.728**	**11.5**
4083.90	V48b	0.0418	13.8	0.0701	23.2
4087.15	V48c	0.0580	18.6	0.0685	21.9
4089.29	V48a	0.1475	13.9	0.2059	19.1
4275.55	V67a	0.2096	16.2	0.2434	18.8
4282.96	V67c	0.0587	12.6	–	–
4303.82	V53a	0.0930	18.1	0.0684	13.3
4466.42	V86b	–	–	0.0387:	35.9:
4609.44	V92a	0.0852	14.3	0.0603	10.1
3d–4f		**0.694**	**15.2**	**0.717**	**17.6**
Adopted			**12.9**		**12.3**

Table 6 – *continued*

λ_0 (Å)	Mult.	I_{obs}	O^{2+}/H^{+} (10^{-4})
		NGC 2440	
4638.86	V1	0.2840:	24.0:
4641.81	V1	0.2051:	7.14:
4649.13	V1	0.1266	2.32
4650.84	V1	0.0510	4.48
4661.63	V1	0.0346	2.38
4676.24	V1	0.0710:	5.81:
V1 3s ^{4}P–3p ^{4}D^o		**0.212**	**2.63**
4414.90	V5	0.0472	6.91
4416.97	V5	0.0380	10.0
V5 3s ^{2}P–3p ^{2}D^o		**0.085**	**8.02**
4153.30	V19	0.0260	3.35
V19 3p ^{4}P^o–3d ^{4}P		**0.026**	**3.35**
Adopted			**5.23**

similar fit to a subset of the nebulae discussed here. A linear fit to the 16 PNe plotted in the bottom panel of Fig. 3 yields

$$\mathrm{ADF}\left(\frac{\mathrm{O}^{2+}}{\mathrm{H}^{+}}\right) = (0.224 \pm 0.053) + (21.6 \pm 2.4) \times 10^{-5}\Delta T, \quad (2)$$

with a linear correlation coefficient of 0.92.

The correlations of the ADFs for doubly ionized C and O with the difference between the [O III] and BJ nebular temperatures are significant, because they provide a strong observational indication that the nebular thermal structure is intimately tied to the problem of discordant – ORL versus CEL – abundance determinations.

4.2 Abundance discrepancy factors versus PN intrinsic surface brightnesses

Nebular surface brightness can be considered as an evolutionary parameter, because for an expanding nebula it decreases as the nebula ages and the mean density drops. Garnett & Dinerstein (2001a) found that, for a sample of about 12 PNe, the magnitude of the ADF(O^{2+}/H^{+}) discrepancy factor was inversely correlated with the mean nebular Balmer line surface brightness, 'suggesting that the abundance problem is a function of PN evolution'. In Fig. 4 we have plotted ADF(O^{2+}/H^{+}) and ADF(C^{2+}/H^{+}) values, taken from the same sources as used for Fig. 3 (described in Section 4.1), against mean nebular Hβ surface brightnesses, for samples of 21 and 20 PNe, respectively. Here the surface brightness, $S(\mathrm{H}\beta)$, is defined as the flux received per arcsec^2 of the nebula corrected for interstellar extinction. For all galactic PNe, we use nebular angular radii, Hβ integrated fluxes and logarithmic extinction coefficients, $c(\mathrm{H}\beta)^{\mathrm{rad}}$, from (Cahn, Kaler & Stanghellini 1992, hereafter CKS92); for the Cloud PNe, integrated fluxes are from Meatheringham, Dopita & Morgan (1988). For LMC N66, we adopt an angular radius of 1.5 arcsec (Dopita et al. 1993), for LMC N141 we adopt 0.30 arcsec (Shaw et al. 2001), while for SMC N87 we adopt 0.23 arcsec (Stanghellini et al. 2003). The ORL/CEL abundance ratios for NGC 6572 were derived from our unpublished ESO 1.52-m observations.

From Fig. 4, we confirm that the ADFs are inversely correlated with the nebular surface brightness. A linear fit to the 21 PNe plotted in Fig. 4 (top) yields

$$\mathrm{ADF}\left(\frac{\mathrm{O}^{2+}}{\mathrm{H}^{+}}\right) = (-3.52 \pm 1.41) - (0.327 \pm 0.113) \times \log S(\mathrm{H}\beta), \quad (3)$$

Table 7. Recombination-line oxygen abundances for Galactic PNe.

	NGC 3242	**NGC 5882**	**NGC 5315**	**NGC 3918**	**NGC 2022**	**NGC 6818**
$10^4 \times O^{2+}/H^+$	6.28	9.70	8.57	5.36	13.01	7.33
$10^4 \times O^{3+}/H^+$	2.05[a]	–	–	–	3.62[a]	2.37[a]
$I(\lambda4632)$	–	–	–	0.150	0.334	0.200
$10^4 \times O^{4+}/H^+$	–	–	–	0.474	1.100	0.641
CEL O^+/O^{2+}	0.0091	0.029	0.098	0.086	0.020	0.090
icf(O)	1.000	1.010	1.332	1.298	1.000	1.000
$10^4 \times O/H$	**8.39**	**10.08**	**12.53**	**12.32**	**17.99**	**11.00**
	NGC 3132	**NGC 2440**	**NGC 6302**	**IC 4406**	**IC 4191**	**My Cn 18**
$10^4 \times O^{2+}/H^+$	8.15	5.23	3.28	7.06	12.92	6.43
$10^4 \times O^{3+}/H^+$	–	2.56[a]	–	–	–	–
$I(\lambda4632)$	–	0.300	0.228	–	–	–
$10^4 \times O^{4+}/H^+$	–	1.01	0.784	–	–	–
CEL O^+/O^{2+}	0.894	0.285	0.092	0.471	0.041	0.590
icf(O)	1.020	1.000	1.672	1.040	1.070	1.003
$10^4 \times O/H$	**15.74**	**10.29**	**7.30**	**10.80**	**14.39**	**10.24**

[a]From the Liu & Danziger (1993a) analysis of O III V8 λ3265.

Table 8. Elemental C, N, O abundances by number, derived from CELs and ORLs, in units where $\log N(\mathrm{H}) = 12.0$. All values are for the entire nebulae, except NGC 6302, 6818, My Cn 18 and IC 4406 where values are from fixed-slit observations; CEL results are from Paper I.

PN	C		N		O	
	ORL	CEL	ORL	CEL	ORL	CEL
NGC 2022	9.17	8.33	8.84	7.46	9.26	8.66
NGC 2440(I)	9.01	8.37	9.01	8.16	9.01	8.39
NGC 3132	9.11	8.50	8.91	8.37	9.20	8.82
NGC 3242	8.93	8.14	8.38	7.53	8.92	8.52
NGC 3918	8.88	8.64	8.41	8.02	9.09	8.86
NGC 5315	8.86	8.33	8.77	8.52	9.10	8.79
NGC 5882	8.65	8.18	8.46	8.18	9.00	8.69
NGC 6302(I)	8.74	7.89	9.05	8.52	8.86	8.40
NGC 6818	8.89	8.41	8.80	7.74	9.04	8.71
IC 4191	8.81	–	8.91	7.59	9.16	8.78
IC 4406	9.05	8.56	8.56	8.32	9.03	8.76
My Cn 18	8.78	–	$\geqslant$9.31	8.34	9.01	8.75
SMC N87	8.88	8.58	–	7.55	8.48	8.03
LMC N66	–	7.52	–	7.99	9.54	8.50
LMC N141	8.88	8.30	–	7.95	8.71	8.29
KB94 non-type I[a]	–	8.81	–	8.14	–	8.69
KB94 type I[a]	–	8.48	–	8.72	–	8.65
Solar[b]	–	8.39	–	7.97	–	8.69

[a]From Kingsburgh & Barlow (1994).
[b]Solar photospheric abundances from Grevesse et al. (1996), except O and C which are from Allende Prieto et al. (2001) and Allende Prieto et al. (2002), respectively.

with a linear correlation coefficient of −0.55, while a linear fit to the 20 PNe plotted in Fig. 4 (bottom) yields

$$\mathrm{ADF}\left(\frac{\mathrm{C}^{2+}}{\mathrm{H}^+}\right) = (-2.88 \pm 1.00) - (0.285 \pm 0.080) \times \log S(\mathrm{H}\beta), \quad (4)$$

with a linear correlation coefficient of −0.64, i.e. the fit and correlation coefficient is not very strong for ADF(O^{2+}/H^+) (Fig. 4, upper), being quite better for ADF(C^{2+}/H^+) (Fig. 4, lower).

4.3 Abundance discrepancy factors versus PN absolute radii

Fig. 5 plots the ADF(O^{2+}/H^+) and ADF(C^{2+}/H^+) ADFs versus nebular absolute radii. For all galactic PNe, we have used the absolute radii quoted by CKS92, except for NGC 3132 where the radius was derived assuming a distance to the nebula of 600 pc (Sahu & Desai 1986) and an angular radius of 22.5 arcsec (CKS92). For the Cloud PNe, we adopted the following: for LMC N66, a radius of 0.324 pc (Dopita et al. 1993); for LMC N141, a radius of 0.074 pc, adopting a nebular angular radius of 0.30 arcsec (Shaw et al. 2001) and assuming the same distance to the LMC (50.6 kpc) as adopted by Dopita et al. (1996); finally, for SMC N87, a radius of 0.067 pc, based on the (photometric) optical *Hubble Space Telescope* (*HST*) diameter of 0.45 arcsec (Stanghellini et al. 2003) and assuming a distance to the SMC of 60 kpc.

We see that a positive linear correlation exists between ADF(C^{2+}/H^+) and the absolute nebular radius for 20 PNe (Fig. 5, bottom), which can be fitted by

$$\mathrm{ADF}\left(\frac{\mathrm{C}^{2+}}{\mathrm{H}^+}\right) = (0.242 \pm 0.121) + (5.51 \pm 1.35)\, R, \quad (5)$$

with a linear correlation coefficient of 0.69.

No such correlation is obvious regarding ADF(O^{2+}/H^+) (Fig. 5, top).

4.4 Temperature differences versus PN radii and surface brightnesses

So far we have seen that ADFs are: (i) positively correlated with the difference between the [O III] forbidden-line and BJ temperatures; (ii) weakly correlated with decreasing intrinsic nebular surface brightness; (iii) positively correlated with the absolute PN radii

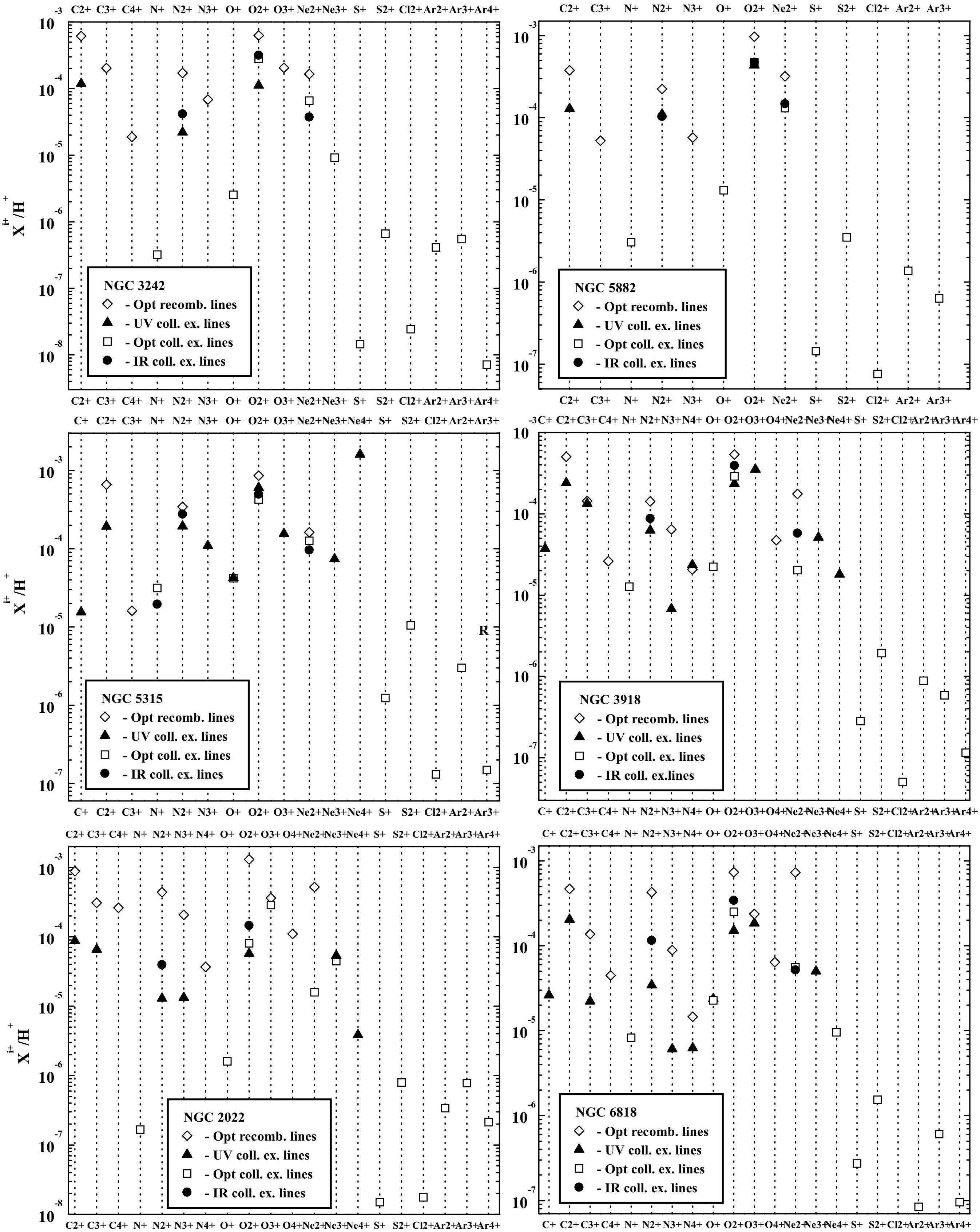

Figure 1. Ionic abundances derived from ORLs, and from UV, optical and IR CELs. In these and subsequent graphs, the plotted values are for the entire nebulae originating from ground-based scanning optical spectroscopy and wide aperture, *IUE*, *ISO* and *IRAS* observations, except for NGC 6302, 6818, IC 4406 and My Cn 18, where abundances from ORLs and optical CELs have been derived from fixed-slit spectra.

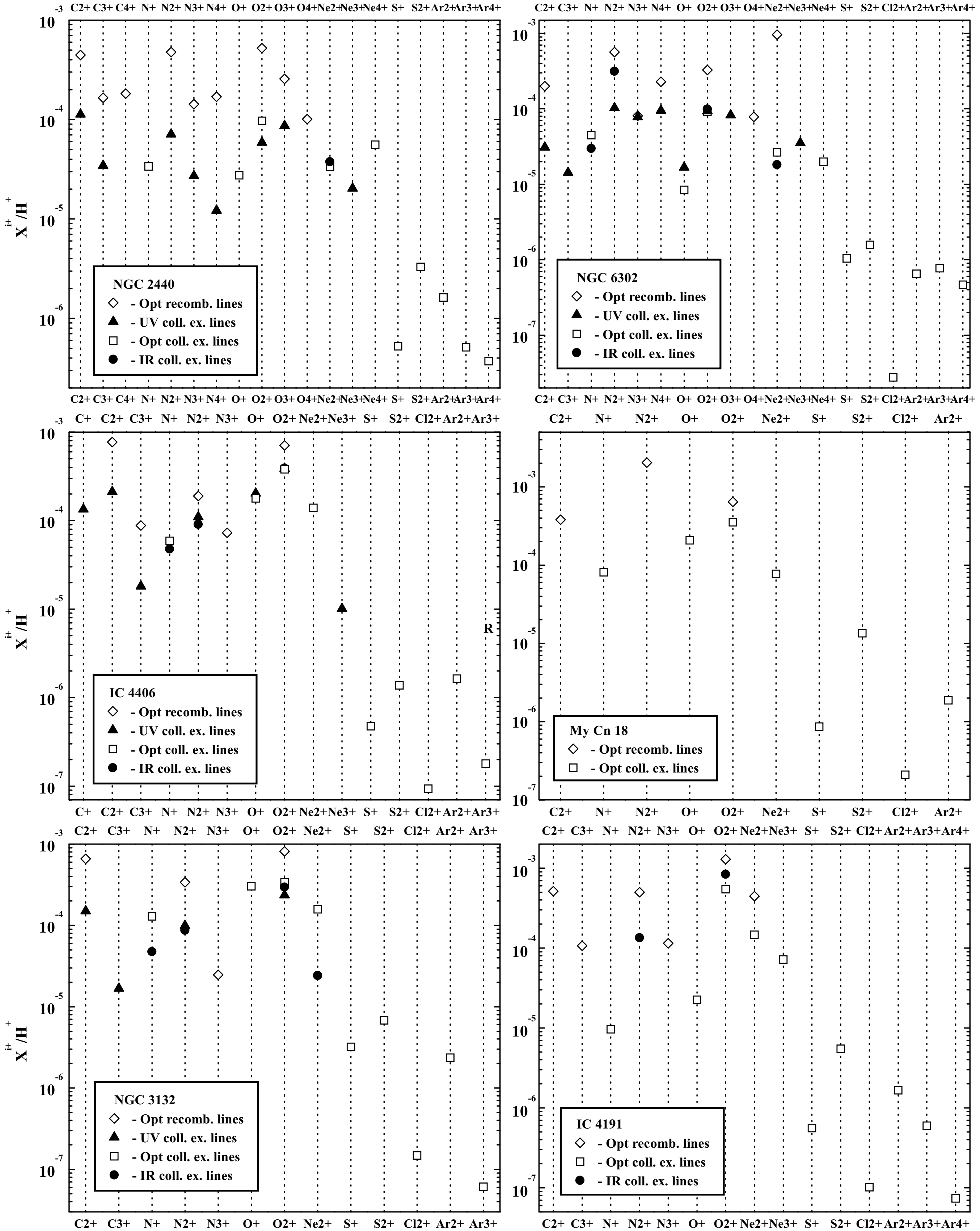

Figure 1 – *continued*

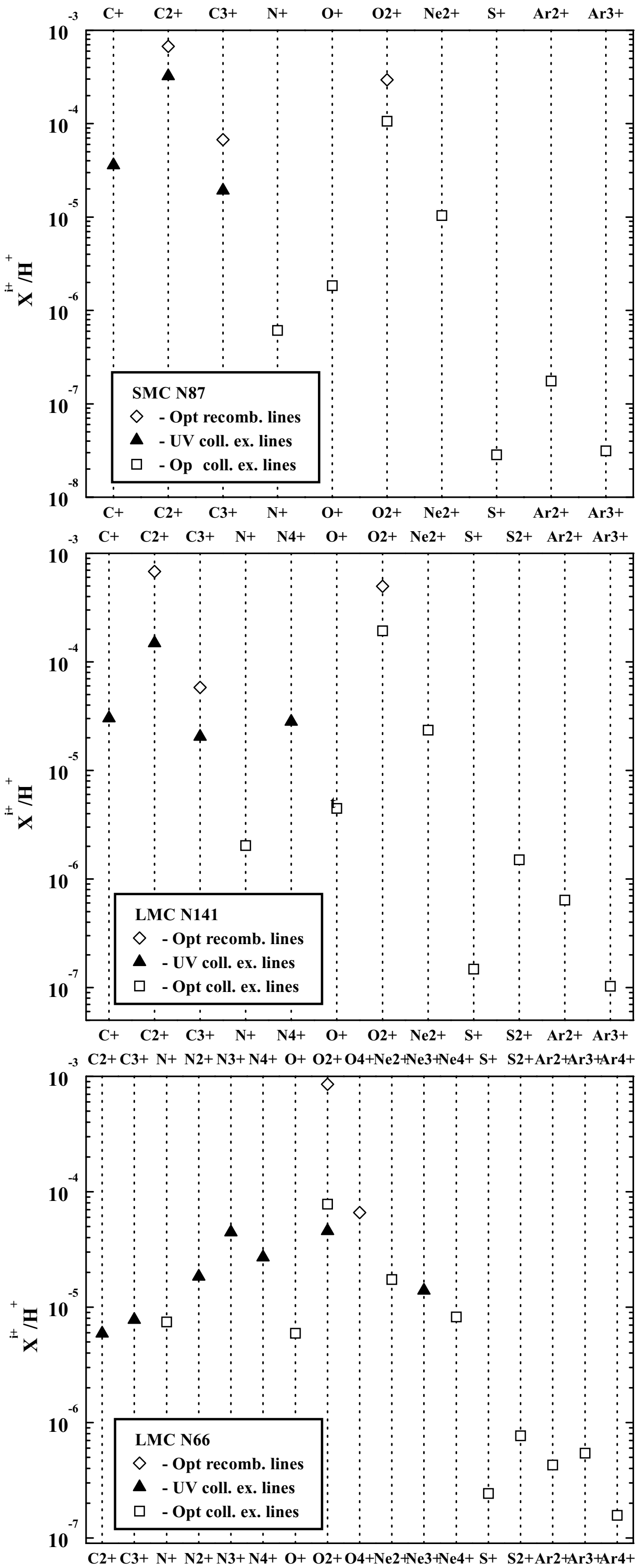

Figure 1 – *continued*

[for the case of ADF(C^{2+}/H^+) mostly]. Therefore, it is not surprising to find that the aforementioned temperature difference is also inversely correlated with $S(H\beta)$ and positively correlated with the absolute nebular radii (Fig. 6).

A linear fit to the 25 nebulae plotted in Fig. 6 (left) yields

$$\Delta T = (-17.6 \pm 6.1) \times 10^3 - (1517 \pm 481) \log S(H\beta), \qquad (6)$$

with a linear correlation coefficient of −0.55.

The relation between ΔT and the nebular radii for the same 25 objects (Fig. 6, right) can be fitted by,

$$\Delta T = (-853 \pm 744) + (28.1 \pm 7.6) \times 10^3 R, \qquad (7)$$

which has a linear correlation coefficient of 0.61.

In Fig. 6, apart from the 11 nebulae whose BJ temperatures were measured in the context of this study, we also included data for six objects published previously (see Section 4.1 for details on these), along with data for a further eight nebulae whose BJ and [O III] temperatures were presented by LD93b.

5 EFFECTS OF NEBULAR DENSITY AND TEMPERATURE VARIATIONS

5.1 Density inhomogeneities

In Paper I, nebular electron densities derived from various diagnostic ratios were presented. It was shown that the low critical density [O III] 52- and 88-μm lines yield electron densities that are, on average, a factor of 6 lower than those derived from the optical [Ar IV] and [Cl III] doublets, which have much higher critical densities. Given that the [O III], [Ar IV] and [Cl III] lines arise from regions of similar ionization degree,[2] this result points to the presence of strong density variations within the nebulae. The effects of such variations on the O^{2+}/H^+ and N^{2+}/H^+ abundance ratios derived from the far-IR lines were discussed in Paper I in the context of the Rubin (1989) examination of the effects of varying N_e on nebular abundances. The general conclusion from Rubin's work is that when there are variable density conditions, the intensity ratios of forbidden lines with low critical densities relative to $H\beta$ (or any recombination line with a volume emissivity $\propto N_e^2$) will generally underestimate the true ionic abundances. We have seen that, in accord with these theoretical predictions, abundances from far-IR lines are, in general, underestimated relative to UV and optical values (which are subject to smaller bias due to their higher N_{cr}), when the 'low' [O III] 52-μm/88-μm densities are adopted for the calculations. In contrast, we have seen that when higher N_e are adopted (intermediate or equal to the [Ar IV] and [Cl III] densities), the inferred abundances from the far-IR lines become compatible with those derived from the UV and optical indicators (see Fig. 1 of this paper and fig. 3 of Paper I); with the exception of the high critical density [Ne III] 15.5-μm line which is not affected by such modest density variations.

In all cases, however, and even after accounting for modest density variations, the CEL abundances derived from UV, optical or IR lines remain consistently lower than the ORL values (Fig. 1). Viegas & Clegg (1994) have shown that dense clumps with $N_e > 10^6$ cm^{-3} can have a substantial effect on the derived [O III] forbidden-line temperature, via collisional suppression of the nebular λλ4959, 5007 lines. In this way, the observationally derived T_e([O III]) could be significantly overestimated and CEL abundances accordingly underestimated. In their analysis of the extreme nebula NGC 6153, Liu et al. (2000) discussed the case for the existence of dense condensations with a very small filling factor as a potential explanation for the large ORL/CEL abundance discrepancies. They concluded

[2] The ionization potential of O^+ (= 35.1 eV) falls between those of Cl^+ (= 23.8 eV) and Ar^{2+} (= 40.7 eV).

Table 9. Ionic ORL/CEL ADFs. Parenthesized values are from Rola & Stasińska (1994).

PN	ADF(C^{2+})	ADF(C^{3+})	ADF(N^{2+})		ADF(N^{3+})	ADF(N^{4+})		ADF(O^{2+})		ADF(O^{3+})	ADF(Ne^{2+})
	ORL/UV	ORL/UV	ORL/UV	ORL/IR	ORL/UV	ORL/UV	ORL/OPT	ORL/UV	ORL/IR	ORL/UV	ORL/OPT
NGC 2022	10. (9.1)	4.7	34.0	11.0	15.0	–	16.0	23.0	9.0	1.3	33.0
NGC 2440	4.0 (2.5)	4.8	6.7	–	5.3	14.0	5.4	8.9	–	–	2.9
NGC 3132	4.4	–	3.4	3.9	–	–	2.4	3.5	2.8	–	–
NGC 3242	5.2 (5.5)	–	7.8	4.1	–	–	2.2	5.7	2.0	–	2.5
NGC 3918	2.1 (3.4)	1.1	2.3	1.6	9.5	0.9	1.8	2.3	1.4	–	8.7
NGC 5315	3.4	–	1.8	1.2	–	–	2.0	1.4	1.7	–	1.3
NGC 5882	2.9	–	1.5	2.2	–	–	2.1	2.2	2.1	–	2.3
NGC 6302	6.5 (3.3)	–	5.5	1.8	1.0	2.4	3.6	3.5	3.3	–	36.
NGC 6818	2.3 (1.3)	6.2	12.0	3.7	14.0	2.3	2.9	4.9	2.1	1.3	13.0
IC 4191	–	–	–	3.7	–	–	2.4	–	1.5	–	3.0
IC 4406	3.7	4.9	1.7	2.1	–	–	1.9	1.8	1.8	–	–
My Cn 18	–	–	–	–	–	–	1.8	–	–	–	–
SMC N87	2.1	3.5	–	–	–	–	2.8	–	–	–	–
LMC N66	–	–	–	–	–	–	11.0	19.0	–	–	–
LMC N141	4.6	2.9	–	–	–	–	2.6	–	–	–	–
NGC 4361	15.0	4.0	–	–	–	–	–	–	–	–	–
NGC 6153	9.0 (9.7)	–	3.3	9.0	–	–	9.2	–	7.3	–	11.0
NGC 6572	2.1 (1.1)	–	–	–	–	–	1.5	–	3.9	–	–
NGC 6644	2.8 (2.8)	–	–	–	–	–	1.9	–	–	–	–
NGC 7009	4.1 (5.3)	3.2	3.2	7.1	–	–	5.0	–	5.9	–	–
M 1-42	23.0	–	–	8.2	–	–	22.0	–	11.0	–	17.0
M 2-36	4.8	–	–	5.6	–	–	6.9	–	5.6	–	7.7

Table 10. Comparison of C/O abundance ratios from CELs and ORLs. Parenthesized values are from Rola & Stasińska (1994). See Section 3.3 for explanation when two values are listed for the CEL C/O ratio.

PN	C^{2+}/O^{2+} λ4267/O II	C^{2+}/O^{2+} λ1908/λ1663	C^{2+}/O^{2+} λ1908/λ4959+λ5007	C^{2+}/O^{2+} λ1908/52+88 μm	ORL C/O	CEL C/O
NGC 2022	0.68	1.52	1.08 (1.21)	0.60	0.82	0.47
NGC 2440	0.85	1.93 (1.23)	1.16 (0.94)	–	0.99	0.96
NGC 3132	0.81	0.64 (0.63)	0.44 (1.68)	0.51	0.81	0.48
NGC 3242	0.98	1.06 (0.66)	0.42 (0.62)	0.37	1.01	0.42|1.05
NGC 3918	0.94	1.03 (1.15)	0.83 (0.90)	0.61	0.60	0.60
NGC 5315	0.77	0.32 (0.31)	0.45 (0.27)	0.39	0.58	0.34
NGC 5882	0.39	0.30	0.27	0.27	0.44	0.27
NGC 6302	0.61	0.33 (0.38)	0.34 (0.39)	0.31	0.75	0.31
NGC 6818	0.64	1.35 (1.45)	0.81 (1.28)	0.60	0.70	0.49|0.64
IC 4191	0.40	–	–	–	0.45	–
IC 4406	1.09	0.55	0.58	0.54	1.25	0.62
My Cn 18	0.59	–	–	–	0.59	–
SMC N87	2.28	–	3.04	–	2.52	3.49
LMC N66	–	0.13	0.08	–	–	0.10
LMC N141	1.38	–	0.77	–	1.48	1.02
Solar [a]	–	–	–	–	–	0.50

[a]Solar oxygen and carbon abundances are taken from Allende Prieto et al. (2001) and Allende Prieto et al. (2002), respectively.

that such dense clumps would have a different effect on different CEL lines. In particular, they found that in the increased density environment of the condensations, most IR and optical CELs would be collisionally suppressed, accounting for the abundance ratios, thus covering part of the distance from the ORL values. On the other hand, however, the abundances derived from the high critical density UV CELs, using the downward corrected electron temperatures that result from allowing for the collisional suppression of the λλ4959, 5007 lines, would become so enhanced as to exceed the ORL abundance results. The conclusion in this case is that the existence of dense condensations is not in itself a sufficient solution to the problem, because it requires the discrepancies to be correlated with the critical densities of the various CELs, something not indicated by the observations.

5.2 Temperature fluctuations

Peimbert (1967) first proposed that in the presence of temperature fluctuations within nebulae, adoption of the [O III] (λ4959 + λ5007)/λ4363 line ratio as a standard thermometer would result in

Table 11. Comparison of N/O abundance ratios from CELs and ORLs. See Section 3.3 for explanation when two values are listed for the CEL N/O ratio.

PN	N^{2+}/O^{2+} NII/OII	N^{2+}/O^{2+} λ1750/λ1663	N^{2+}/O^{2+} λ1750/λ4959+λ5007	N^{2+}/O^{2+} 57 μm/52+88 μm	ORL N/O	CEL N/O
NGC 2022	0.34	0.23	0.16	0.27	0.38	0.13
NGC 2440	0.91	1.21	0.73	–	0.99	0.59|1.09[a]
NGC 3132	0.42	0.42	0.29	0.30	0.51	0.36|0.43
NGC 3242	0.27	0.20	0.08	0.13	0.29	0.10|0.26
NGC 3918	0.26	0.27	0.22	0.22	0.21	0.23
NGC 5315	0.40	0.32	0.45	0.56	0.47	0.54|0.42
NGC 5882	0.23	0.25	0.23	0.22	0.29	0.33
NGC 6302	1.72	1.10	1.12	3.16	1.53	1.34
NGC 6818	0.58	0.22	0.14	0.34	0.58	0.16|0.21
IC 4191	0.39	–	–	0.16	0.56	0.06|0.17
IC 4406	0.27	0.28	0.29	0.23	0.34	0.36|0.34
My Cn 18	3.16	–	–	–	⩾2.0	0.39
SMC N87	–	–	–	–	–	0.33
LMC N66	–	0.55	0.34	–	–	0.41
LMC N141	–	–	–	–	–	0.45
Solar[a]	–	–	–	–	–	0.19

[a]Solar oxygen abundance taken from Allende Prieto et al. (2001); solar nitrogen abundance from Grevesse et al. (1996).

the underestimation of elemental abundances as derived from CELs, because that line ratio would be biased towards high-temperature nebular regions. Generally speaking, if variations in electron temperature exist along the line of sight through a nebula, abundance ratios derived from the ratio of a CEL to a recombination line (e.g. the most commonly used recombination line, Hβ) will be underestimated, while those derived from a pure recombination-line ratio should be almost insensitive to T_e and thus largely unaffected by any incorrect assumptions regarding the nebular temperature distribution.

Peimbert (1971) found possible evidence for the existence of such temperature fluctuations, by comparing for three PNe the temperature derived from the ratio of the Balmer continuum jump to the intensity of Hβ with that obtained from the [O III] nebular to auroral CEL ratio. He found that the latter temperatures were higher than T_e(BJ). This result has been supported by further observations of more PNe (e.g. LD93b). The BJ temperatures that we presented for 12 PNe in table 7 of Paper I were also systematically lower than the corresponding T_e([O III]) values presented there.

The concept of temperature fluctuations in a chemically homogeneous nebula has been invoked several times as a promising cause of the ORL/CEL abundance discrepancy problem, pertaining to both discrepant C^{2+}(λ4267)/H^+ and O^{2+}/H^+ ORL abundance ratios. For instance, Peimbert et al. (1993) proposed that spatial temperature fluctuations with an amplitude of ∼20 per cent around a mean value would reconcile the factor of 1.55 discrepancy between the ORL and CEL O^{2+}/H^+ abundances in the PN NGC 6572. Peimbert, Luridiana & Torres-Peimbert (1995) have derived electron temperatures for a sample of nebulae from the C III] λ1908/C II λ4267 ratio and have shown that they are generally lower than T_e([O III]). On account of this, they argued that, in order to explain the discrepancy between the C^{2+}(λ4267)/O^{2+}(λ5007) and C^{2+}(λ1908)/O^{2+}(λ5007) values in PNe published by Rola & Stasińska (1994), large temperature fluctuations were needed. They also recommended the adoption of $T_e(C^{2+})$ rather than T_e([O III]) when deriving ionic abundances from CELs and concluded that due to their insensitivity to temperature variations, abundances derived from pure recombination-line ratios are more reliable.

However, the validity of the C III] λ1908/C II λ4267 ratio (or even that of the C IV λ1549/C III λ4650 ratio) as a reliable nebular thermometer is ambiguous, because there is evidence that, for PNe which exhibit non-uniform, inhomogeneous abundances, the C II λ4267 ORL and C III] λ1908 CEL do not originate in the same gaseous component. Harrington & Feibelman (1984) argued that such is the case for the hydrogen-deficient material which exists at the centre of the PN A30 in the form of condensations. Subsequent, detailed photoionization modelling of *HST* and ground-based spectra of several of the knots in A30 (Borkowski et al. 1993; Ercolano et al. 2003) has confirmed that the ORLs and CELs originate from different regions of the knots.

We have investigated our results for evidence that temperature fluctuations may contribute to the observed abundance discrepancies. The major premise of this scenario is that ionic abundances derived from the intensity ratio of two lines with very different temperature dependences, e.g. I([O III] λ1663)/I(Hβ), will be severely biased if an incorrect T_e is adopted in calculating line emissivities. Because, on average, $T_e(\mathrm{BJ}) \leqslant T_e$([O III]), and because the standard practice is to use the [O III] optical line ratio temperature in order to calculate both the emissivities of CELs and of Hβ, the possibility of systematically underestimating CEL abundances is there. Should then ORL abundances that are insensitive to temperature bias be trusted more and if so why do they point towards heavy element overabundances in most nebulae? One way to try to answer this question is to examine the effects of changing the adopted T_e on ionic abundances derived from CELs that have different temperature dependences.

In the current study, the standard electron temperature from the [O III] (λ4959 + λ5007)/λ4363 line ratio was adopted in order to derive all ionic abundances of doubly ionized species. If we suppose, however, that the T_e pertinent to the nebular zones where doubly ionized species exist is lower than that, e.g. that it may be as low as the H I BJ temperature, then the ionic abundances derived from CELs would all be underestimated by our adoption of $T_e = T_e$([O III]), but not all by the same factor. Abundances derived from high-excitation energy transitions, such as O III] λ1663 ($E_{ex} \simeq 86$ kK), N III] λ1751 ($E_{ex} \simeq 82$ kK) or C III] λ1908 ($E_{ex} \simeq 75$ kK), would be

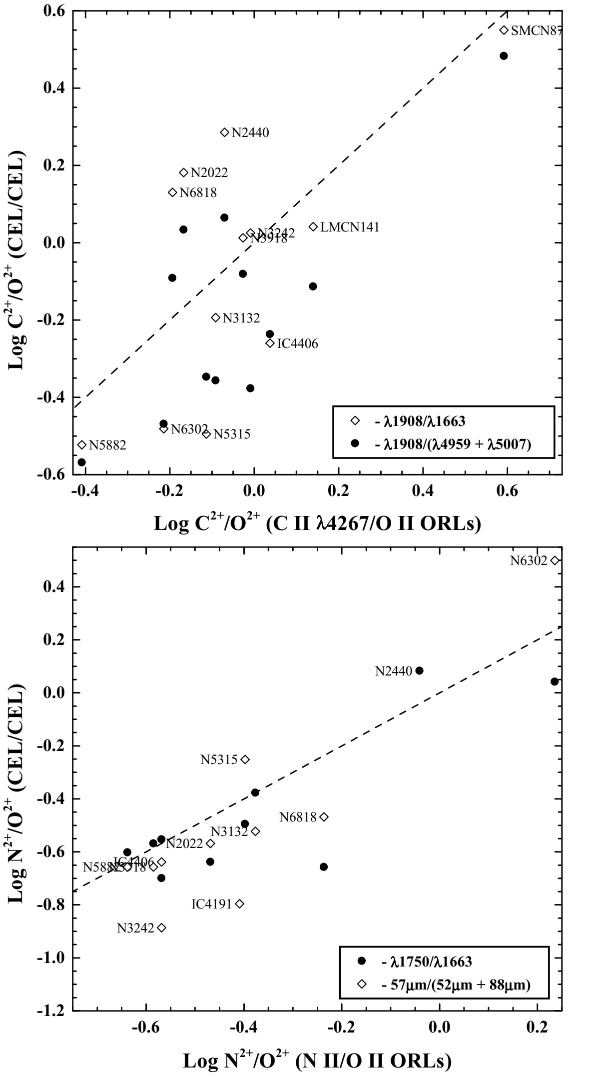

Figure 2. Comparison of the C^{2+}/O^{2+} (top) and N^{2+}/O^{2+} (bottom) ionic abundance ratios derived from ORLs, and from UV, optical and far-IR CELs. Data points with identical *x*-axis values share the same label. The dashed lines have a slope of unity.

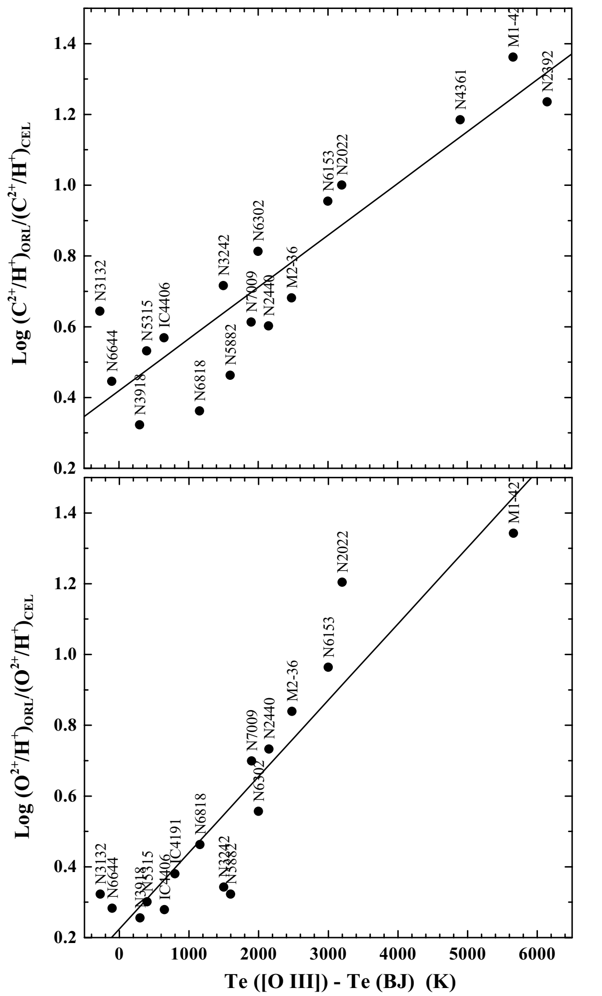

Figure 3. Top: ORL/CEL ionic ADFs for C^{2+} plotted against the difference between the [O III] and BJ electron temperatures. Bottom: the same for the O^{2+} ratios. The solid lines are the linear fits of equations (1) and (2); see text for details.

underestimated more relative to those derived from transitions that have a lower temperature sensitivity, such as the [O III] λλ4959, 5007 nebular lines ($E_{\rm ex} \simeq 29$ kK). Our results show however (Table 9) that all CEL C^{2+}, N^{2+} and O^{2+} abundances are systematically lower than those derived from ORLs, by rather similar factors.

For instance, the average C^{2+}λ4267/λ1908 ADF for 18 nebulae is 5.4, while the O^{2+}(ORL/λ4959 + λ5007) ADF is 5.1; also the O^{2+} ORL/λ1663 ADF for 10 nebulae is 5.7 (Table 9). This apparent uniformity cannot be reconciled with the different behaviour that one would expect amongst the discrepancy ratios in the case of temperature fluctuations of the type envisaged by Peimbert. We would expect the C^{2+} ORL/CEL ADFs to be greater than that for O^{2+}, because the 75-kK excitation energy of the upper levels of the λ1908 doublet exceeds the 62-kK excitation energy of the upper level of the λ4363 transition. However, in the extreme nebula NGC 2022 the ADF for C^{2+} is 10, but that for O^{2+} is 16, i.e. the opposite of that expected. In the other extreme nebulae NGC 6153 (Liu et al. 2000) and M1-42 (Liu et al. 2001b), the corresponding factors are almost equal. Similarly, we would expect the C^{3+} ORL/CEL ADF to be greater than that for C^{2+}, due to the higher excitation energy of the C IV λ1549 resonant doublet ($E_{\rm ex} \simeq 93$ kK), relative to that of C III] λ1908 ($E_{\rm ex} \simeq 75$ kK); however, this is not the case for the nine PNe with both C^{2+}λ4267/λ1908 and C^{3+} ORL/λ1549 ADFs documented, where, on average, these ADFs are 5.3 and 3.9, respectively.

Having just seen that in the presence of temperature fluctuations we would expect ADF(C^{2+}/H^+), as defined in the previous section, to be affected more by errors in $T_{\rm e}$ than in ADF(O^{2+}/H^+), our fits (equations 1 and 2) show that actually it may well be that the opposite is true, judging from the slightly steeper ADF(O^{2+}/H^+) function (Fig. 3). This behaviour of the two discrepancy factors conflicts with that expected for temperature fluctuations of the standard type.

Probably, however, the most serious obstacle to the classical temperature fluctuation hypothesis lies with the IR abundance results. Inspection of Fig. 1 and Table 9 shows that the ORL/CEL ADFs for CEL abundances obtained from the far-IR [O III] and [N III] lines are in line with those from the optical and UV CELs, i.e. there is no correlation whatsoever with the very low $E_{\rm ex}$ ($\lesssim$1000 K) of IR transitions. As we mentioned in Section 3.2, very satisfactory agreement is reached amongst UV, optical and IR CEL O^{2+}/H^+ ADFs, while the same is also true for N^{2+}/H^+ and Ne^{2+}/H^+; this would

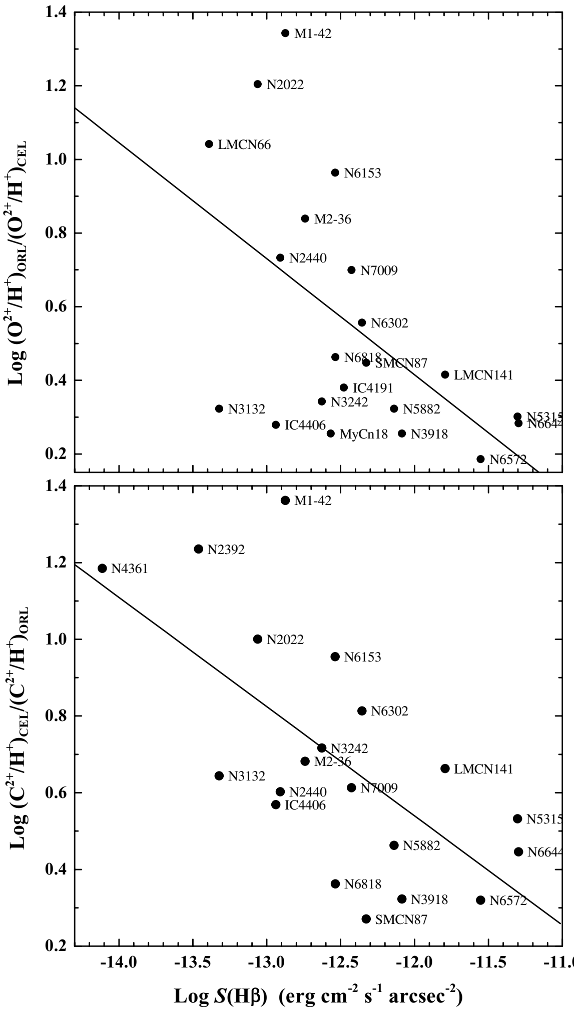

Figure 4. O^{2+}/H^{+} (top) and C^{2+}/H^{+} (bottom) ADFs, plotted against nebular Hβ surface brightness. The solid lines are the linear fits discussed in the text.

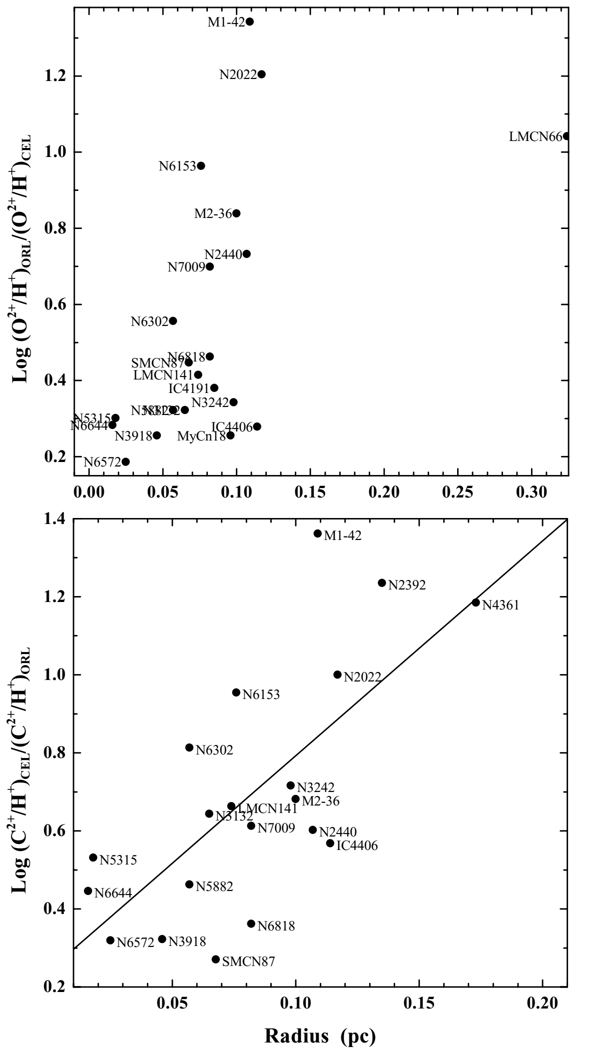

Figure 5. O^{2+}/H^{+} (top) and C^{2+}/H^{+} (bottom) ADFs, plotted against nebular radius. The solid line in the lower plot is the linear fit discussed in the text.

not be the case in the presence of strong temperature fluctuations in a chemically homogeneous nebula.

Ruiz et al. (2003) and Peimbert et al. (2004) have presented deep optical echelle spectra of NGC 5307 and 5315, respectively, deriving O^{2+} ADFs of 1.9 and 1.7 for these two PNe (we obtained an optical O^{2+} ADF of 2.0 for NGC 5315; see Table 9). They argued that these ADFs could be explained by classical temperature fluctuations, corresponding to t^2 values of 0.051 and 0.056, respectively. NGC 5307 has no measurements available for its far-IR FS lines, but *ISO* spectra exist for NGC 5315. Peimbert et al. (2004) chose not to use the the 52- and 88-μm [O III] *ISO* LWS line fluxes presented by Liu et al. (2001a), on the grounds that the electron density of 2290 cm^{-3} yielded by the intensity ratio of these two lines lies between the respective critical densities of 3800 and 1800 cm^{-3}. However, in Paper I we found that for NGC 5315 (and for all the other PNe in our sample with electron densities exceeding one or both of these critical densities), the adoption of an electron density given by the mean of the densities from the [Cl III] and [Ar IV] optical doublet ratios gives an O^{2+} abundance from the far-IR FS lines that agrees with the value obtained from the optical forbidden lines.

With regard to this issue, two PNe in our current sample, NGC 3132 [ADF(O^{2+}) = 2.4] and IC 4406 [ADF(O^{2+}) = 1.9], are of key importance, because their far-IR [O III] doublet ratio densities of 355 and 540 cm^{-3} (Paper I) are well below the critical densities of the two far-IR lines (as are the electron densities derived for these two nebulae from the various optical doublet ratios; see table 6 of Paper I). Thus, there should be no objection to the derivation of O^{2+} abundances from the far-IR [O III] lines for these nebulae. Inspection of table 9 of Paper I shows that for NGC 3132 the O^{2+} abundance derived for the far-IR FS lines, using the far-IR doublet ratio density, differs by less than 14 per cent from the O^{2+} abundance derived from the optical forbidden lines, while for IC 4406 it differs by less than 3 per cent.

Expressing this another way, the electron temperature of 9900 K derived for both NGC 3132 and IC 4406 from the ratio of their IR to optical [O III] doublet fluxes agrees with the temperatures of 9530 and 10 000 K derived from their [O III] λ4363/(λ5007 + λ4959) ratios (table 7 of Paper I). If the rather typical ADFs of ∼2 derived for these two PNe were caused by temperature fluctuations in a chemically homogeneous medium, then the IR to optical [O III] doublet flux ratio should yield significantly lower temperatures than the much more temperature-sensitive λ4363/(λ5007 + λ4959) ratio. This is not the case, so we conclude that classical temperature fluctuations cannot explain the ADFs of ∼2 found for those two nebulae.

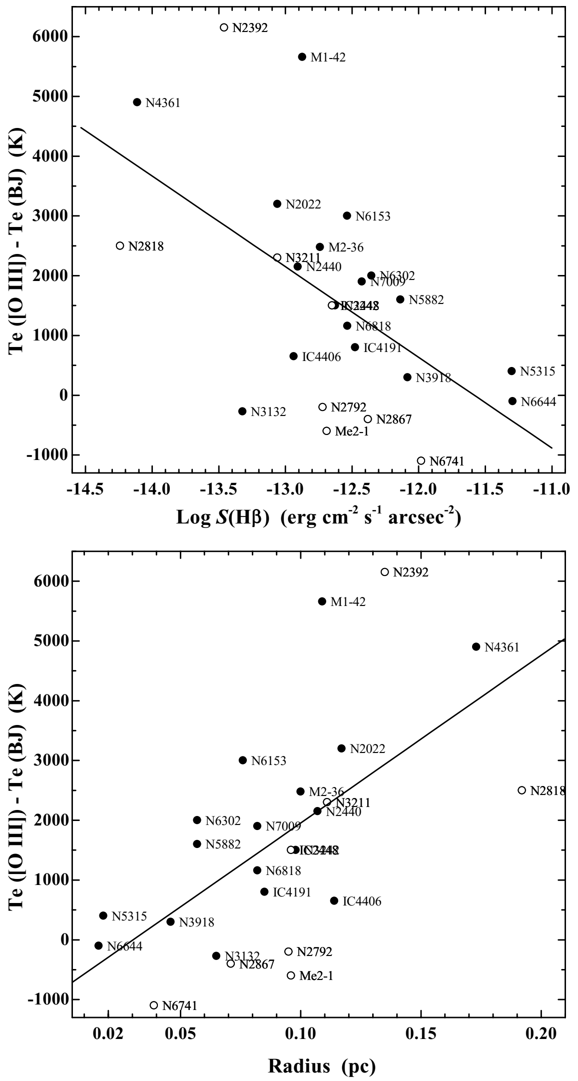

Figure 6. The difference between the nebular electron temperatures derived from the [O III] nebular to auroral forbidden-line ratio, T_e([O III]), and from the nebular Balmer continuum discontinuity, T_e(BJ), is plotted against the intrinsic nebular Hβ surface brightness (top) and absolute radius (bottom). Open circles data are from LD93b. The solid lines are the linear fits discussed in the text.

6 EVIDENCE FOR COLD PLASMA FROM ORL ELECTRON TEMPERATURES

6.1 Electron temperatures from He I ORL ratios

The weak temperature sensitivity of several He I recombination lines was used by Liu (2003) who derived He^+ electron temperatures for five PNe with particularly high O^{2+} ADFs. He found that both the value of T_e(He I) and the ratio of T_e(He I)/T_e([O III]) decreased systematically with increasing nebular ADF, with T_e(He I) ranging from 5380 K for NGC 7009 (ADF = 4.7) down to 2310 K for M1-42 (ADF = 22) and as low as 775 K for Hf 2-2 (ADF = 84). This provided observational support for the presence of regions of cold plasma within these high-ADF nebulae.

It is of interest to investigate what patterns might be shown by the lower-ADF PNe in the current sample, so we have derived He I electron temperatures using the curves presented by Liu (2003, based on the data of Smits 1996). We used his λ6678/λ4471 curves only, because the λ5876/λ4471 curves have minima between 6000 and 10 000 K, which allow matches to a given line intensity ratio at both low and high temperatures. Column 5 of Table 12 presents the dereddened λ6678/λ4471 flux ratios (from Paper I) and the derived values of T_e(He I) are listed in column 6. Also presented in Table 12 are the nebular electron densities (column 2; adopted from table 6 of Paper I) that were used to interpolate between the density-dependent λ6678/λ4471 curves, as well as the nebular [O III] and hydrogen BJ electron temperatures (columns 3 and 4), which are taken from table 7 of Paper I. Very accurate relative flux calibration over the wavelength range spanning the two He I lines is required, because the λ6678/λ4471 ratio varies by only 55–60 per cent between electron temperatures of 1000 and 16 000 K. Despite the stringent requirement on the accuracy of the relative flux calibration over such a wide wavelength range, six of the nine PNe listed in Table 12 show He I electron temperatures within 2000 K of the nebular [O III] electron temperatures: one (NGC 3132) has a He I electron temperature that is 3300 K larger than the [O III] electron temperature, and two of the nebulae, NGC 6818 and IC 4191, yield He I electron temperatures that are respectively 8300 and 7300 K lower than the corresponding [O III] electron temperatures.

6.2 Electron temperatures from O II ORL ratios

In this subsection we present observational evidence that the O II ORLs detected from several of our PNe are emitted from ionized gas which is at temperatures much lower than those derived from either the H I Balmer discontinuity or the [O III] optical forbidden lines, for which values were derived in Paper I (see also the current Table 12). We will make use of the temperature sensitivity of the ratio of the intensities of the λ4089 and λ4649 lines of O II, a technique first used by Wesson, Liu & Barlow (2003), who derived very low electron temperatures for two hydrogen-deficient knots in the PN Abell 30.

The intensities of recombination lines originating from states of different valence orbital angular momentum have different dependences on electron temperature. By comparing the intensity of a line in the O II 4f–3d transition array with one from the 3p–3s array, for example, it is possible to deduce a recombination-line temperature. There are several potential difficulties in using such lines to measure the electron temperature. First, the variation of the intensity ratios with temperature is weak, typically a factor of 2 or 3 when the temperature changes from 300 to 10 000 K, meaning that it is important to ensure that the intensities of the weak recombination lines are determined as accurately as possible. Secondly, the relative intensities may be affected by the distribution of population in the recombining ion ground state, $O^{2+}\ ^3P$ in this case. The available O II recombination coefficients assume that the levels of this term are populated according to their statistical weight (Storey 1994). If the electron density is sufficiently low, this may not be the case, with the energetically higher levels of the $O^{2+}\ ^3P$ state being relatively underpopulated. This has been observed for the low-density H II regions 30 Doradus, LMC N11B and SMC N66 (Tsamis et al. 2003a). Equally, a very low electron temperature would have the same effect.

To attempt to circumvent this second problem, we consider the ratio of intensities of λ4089 from the 4f–3d transition array and λ4649 from the 3p–3s array. These lines originate from the state of highest total angular momentum, J, in each case and should therefore both be mainly populated from the $O^{2+}\ ^3P_2$ level. The published recombination coefficients for these two lines (LSBC and Storey 1994, respectively) are only valid for temperatures $T_e \geqslant 5000$ K.

Table 12. Comparison of CEL and ORL electron temperatures (in K).

Nebula	N_e (cm^{-3})	T_e([O III]) CEL	T_e(BJ) BJ/H11	$I(\lambda6678)$ /$I(\lambda4471)$	T_e(He I) λ6678/λ44713	$I(\lambda4649)$ O II	$I(\lambda4089)$ /$I(4649)$	T_e(O II) λ4089/λ4649	ADF(O^{2+}) ORL/CEL
NGC 2022	1500	15 000	13 200	0.693	$15\,900^{+3500}_{-3300}$	0.333	0.607	$<300^{+2100}_{-2000}$	16
NGC 2440	6000	16 150	14 000	–	–	0.100	0.420	$<300^{+2300}_{-2000}$	5.4
NGC 3132	600	9530	10 800	0.725	$13\,900^{+2500}_{-4300}$	0.195	–	–	2.4
NGC 3242	2000	11 700	10 200	0.774	$10\,000^{+900}_{-2000}$	0.216	0.307[a]	2600^{+2500}_{-1600}	2.2
NGC 3918	5000	12 600	12 300	0.740	$12\,000^{+400}_{-1000}$	0.211	0.288	3650^{+3000}_{-2000}	1.8
NGC 5315	10 000	9000	8600	0.775	$10\,000^{+1200}_{-1500}$	0.344	0.261	5750^{+1000}_{-1750}	2.0
NGC 5882	4000	9400	7800	0.763	$10\,700^{+600}_{-1400}$	0.362	0.230[a]	8700^{+2300}_{-2100}	2.1
NGC 6302	14 000	18 400	16 400	0.671	$15\,100^{+1200}_{-600}$	0.100	–	–	3.6
NGC 6818	2000	13 300	12 100	0.841	5000^{+1000}_{-1000}	0.182	0.300[a]	2900^{+2500}_{-1900}	2.4
IC 4191[b]	10 000	10 700	10 500	0.908	3000^{+1200}_{-800}	0.725	0.284	3900^{+2500}_{-1800}	2.4
IC 4191[c]	10 000	10 000	9200	0.916	2800^{+600}_{-400}	0.572	0.316	2150^{+2500}_{-1400}	2.4
IC 4406	1000	10 000	9350	0.797	8000^{+1800}_{-2000}	0.284	–	–	1.9

[a]Adopted O II 4089.29-Å intensity is after correction for Si IV 4088.85 Å, using the measured intensity of Si IV λ4116.10 Åand adopting a 2:1 flux ratio for the $4s^2S$–$4p^2P^o$ Si IV λ4089/λ4116 doublet components.
[b]Fixed-slit observation.
[c]Scanning-slit observation.

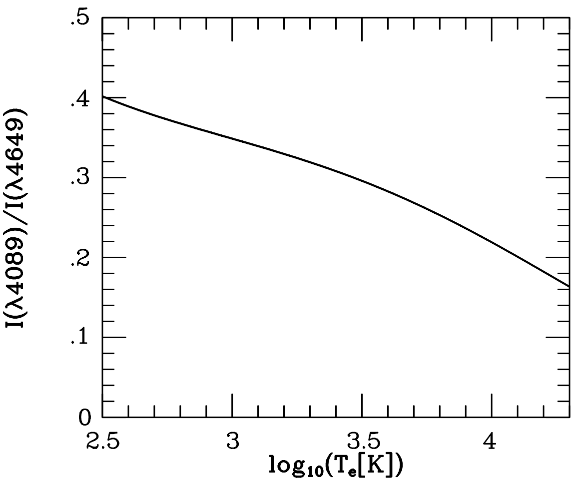

Figure 7. The theoretical intensity ratio for O II λ4089/λ4649 as a function of electron temperature. See Section 6.2 for details.

Because we wish to investigate the very low temperature regime, we have extended the recombination coefficient calculations to temperatures $T_e \geqslant 300$ K. Fig. 7 shows the corresponding intensity ratio for temperatures between 300 and 15 000 K. The calculations could not easily be taken to even lower temperatures due to numerical problems in the recombination coefficient codes.

Measurements of the intensities of λ4089 and λ4649 have been given in Paper I. The λ4089 line is isolated and measurement of the intensity is relatively straightforward.[3] The λ4649 line, on the other hand, is part of a complex blend in which we identify five components: two lines of the O II multiplet V1, λ4649.13 and λ4650.84, and three lines of the C III multiplet V1, λλ4647.42, 4650.25, 4651.47. We have made new five-component fits to this blend for a subset of the PNe, using the known wavelength separations between the lines, assuming that all five lines have the same width as the C II λ4267 line (the strongest heavy element ORL in the spectra), and using the expected intensity ratio of 5 : 3 : 1 for the three C III lines. The resulting λ4089 to λ4649 line ratios and derived electron temperatures are given in Table 12 for the six PNe for which both lines were detected, while the derived relative intensities for λ4649.13 and λ4650.84 can be found in Table B1. Note that the O II electron temperatures presented here in Table 12 supersede those that were listed, without discussion, in table 7 of Paper I.

Inspection of Table 12 shows that two of the eight PNe with derived λ4089/λ4649 O II electron temperatures show values below our 300-K theoretical calculation limit (albeit with rather large estimated errors). The fixed-slit and scanning-slit observations of IC 4191 yield T_e of 3900 and 2150 K, respectively, while NGC 5882 has the highest measured T_e(O II) of 8700 K. It can be shown that these values are reduced further when one takes into account the small contribution to the O II λλ4089, 4649 intensities from the normal nebular gas at T_e([O III]) temperatures. Once this contribution is subtracted from the observed O II intensities, the revised O II ORL ratios (not shown in Table 12) indicate electron temperatures of less than 300 K for six PNe, while for NGC 5315 and 5882 the resulting temperatures are 4350 and 7190 K, respectively. These findings point towards the likely presence of ultracold plasma regions in a large fraction of our sample PNe.

7 DISCUSSION AND CONCLUSIONS

In Sections 3 and 5.2, it was demonstrated that there is no dependence of the magnitude of the nebular ORL/CEL ADFs upon the excitation energy of the UV, optical or IR CEL transition used (see Table 9), indicating that classical (i.e. in a chemically homogeneous medium) nebular temperature fluctuations are not the cause of the observed abundance discrepancies. This reinforces the same conclusion that was reached in Paper I, based there upon the fact that [O III] electron temperatures derived from the ratio of the 52- and 88-μm FS lines to the 4959- and 5007-Å forbidden lines were greater than or comparable to those derived from the ratio of the higher-excitation energy 4363-Å transition to the 4959- and 5007-Å lines – if temperature fluctuations in the ambient nebular material were the cause of

[3] Apart from the cases of NGC 3242, 5882 and 6818, where the detection of weak emission in the 4116.1-Å component of the Si IV $4s^2S$–$4p^2P^o$ λλ4089,4116 doublet (with relative intensities of 0.022, 0.0308 and 0.022, respectively, on a scale where $H\beta = 100$) led us to correct the measured 4089-Å line flux for the presence of Si IV 4088.85 Å, by subtracting twice the measured intensity of the Si IV 4116.10-Å line.

the ORL/CEL abundance discrepancies then the IR line-based ratio should yield lower temperatures. We conclude instead that the main cause of the abundance discrepancies is enhanced ORL emission from cold ionized gas located in hydrogen-deficient clumps inside the nebulae, as first postulated by Liu et al. (2000) for the high-ADF PN NGC 6153.

When nebular heavy element abundances exceed about five times solar, cooling by their collisionally excited IR FS lines is alone sufficient to balance the photoelectric heating from atomic species. Because cooling by the low-excitation IR FS lines saturates above a few thousand Kelvin, nebular electron temperatures in such high-metallicity regions will drop to values of this order, the exact value being determined by the H to heavy element ratios and the input ionizing spectrum. It is therefore physically plausible and self-consistent for the heavy element ORLs that yield enhanced abundances relative to those derived from CELs to also indicate very low electron temperatures for the regions from which they emit.

In their empirical modelling of NGC 6153, Liu et al. (2000) postulated the presence of H-deficient ionized clumps within the nebula that would be cool enough to suppress optical forbidden-line emission and even some IR FS line emission, but which would emit strongly in heavy element recombination lines, due to the inverse power-law temperature dependence of ORL emission. Péquignot et al. (2002) have constructed dual abundance photoionization models of NGC 6153 and M1-42 incorporating H-deficient inclusions and found equilibrium T_e of $\sim 10^3$ K in the H-deficient clumps and $\sim 10^4$ K in the ambient gas, with the H-deficient ionized regions being within a factor of 2 of pressure equilibrium with the ambient nebular gas. Similar conclusions have been reached independently by Tylenda (2003) who constructed composite models of NGC 6153, M1-42 and M2-36. Moreover, Ercolano et al. (2003) were able to explain the ORL and CEL spectrum of a H-deficient knot in A30 only by means of a dual abundance model.

In the models by Péquignot et al. (2002), the H-deficient components contained only ~ 1 per cent of the total ionized mass, so that the overall metallicity of the whole nebula was close to that of the 'normal' high-temperature component. Similar, or lower, mass fractions for the postulated H-deficient clumps in the typical PNe studied here, which have lower ADFs than the extreme cases discussed above, should ensure that their integrated IR FS line emission will not represent a significant perturbation to the integrated IR FS emission from the ambient high-temperature nebular material that forms the majority of the nebular mass, particularly if the H-deficient clump electron densities exceed the rather low critical densities of 500–3000 cm^{-3} that correspond to the [O III] and [N III] IR FS lines which have been investigated in this paper. The strong inverse power-law temperature dependence of ORL emission means that material at a temperature of 500 K will emit an ORL such as O II $\lambda 4649$ 18 times more strongly than at 10^4 K. If 0.5 per cent of the nebular mass was located in 500-K clumps having an electron density 10 times that of the ambient nebular gas, then the integrated ORL emission from the clumps would exceed that from the ambient gas by a factor of 9.

Hydrogen is not expected to be entirely absent in the postulated H-deficient clumps. The steep inverse power-law temperature dependence of its recombination emission from the clumps could be responsible for the strong correlation, discussed in Section 4.1, between the C^{2+} or O^{2+} ADFs and the temperature difference, ΔT, between the [O III] optical forbidden line and H I BJ electron temperatures (see Fig. 3). The correlation between ionic ADFs and decreasing nebular surface brightness (Fig. 4), or increasing absolute nebular radius (Fig. 5), may indicate that the density contrast between the H-deficient clumps and the ambient nebular material increases as the nebula evolves, i.e. that the clump density decreases less than the ambient nebular density does as the nebula expands. Such a situation might arise if the clump ionized gas originates from photoevaporation of dense neutral cores (cometary knots) of the kind found in the Helix nebula (Meaburn et al. 1992; O'Dell, Henney & Burkert 2000) and the Eskimo nebula (NGC 2392; O'Dell et al. 2002). Indeed, the location of NGC 2392 in the ΔT versus $S(\mathrm{H}\beta)$ and ΔT versus radius diagrams (Fig. 6) is consistent with this picture and indicates that NGC 2392 is a candidate high-ADF nebula. In confirmation of this, optical and UV large aperture measurements presented by Barker (1991) for six positions in NGC 2392 yielded $\lambda 4267/\lambda 1908$ C^{2+} ADFs ranging from 7 to more than 24. We thus show NGC 2392 in the ADF(C^{2+}) versus ΔT diagram (Fig. 3) and the ADF(C^{2+}) versus radius diagram (Fig. 5) using a mean C^{2+} ADF of 18 derived for the positions observed by Barker. It would be of interest to obtain deep optical spectra of this nebula in order to examine its heavy element ORL spectrum in detail.

Available spatial analyses of long-slit PN spectra show that ORL/CEL ADFs peak towards the centre of nebulae in the cases of NGC 6153 (Liu et al. 2000) and NGC 6720 (Ring nebula; Garnett & Dinerstein 2001b). An examination of the results presented by Barker (1991) for NGC 2392 shows that the same trend is also present in those data: the inferred ADF(C^{2+}) increases towards the centre of the PN (along the aligned positions 4, 2 and 1; see fig. 1 of that paper). In NGC 6720 especially, the location of peak O II ORL emission does not coincide with the positions of the *HST*-resolved dusty cometary knots, which populate the main shell of the Ring nebula, but is displaced inwards from that of the peak [O III] emission (Garnett & Dinerstein 2001b). We speculate that such an effect could be due to the advanced photoprocessing of knots in the Ring nebula that were overcome by the main ionization front in the past and whose relic material, rich in heavy elements, is now immersed in the He^{2+} nebular zone, being subjected to the intense radiation field of the central star. The question of the possible relationship between the ORL/CEL abundance discrepancy problem and the cometary knot complexes observed in many PNe warrants further investigation.

Ruiz et al. (2003) and Peimbert et al. (2004) have argued against the presence of H-deficient knots in NGC 5307 and 5315 on the grounds that their 34 km s^{-1} resolution echelle spectra did not reveal a difference between the radial velocities or linewidths of the heavy element ORLs and those of the main nebular lines, of the type exhibited by the high-velocity H-deficient knots in the born-again PNe, A30 and A58. We note, however, that the H-deficient knot model that has been invoked to explain the ORL/CEL ADFs of typical PNe makes no specific predictions as to whether the knots should exhibit a different kinematic pattern from the bulk of the nebula. Scenarios for the origin of such knots in 'normal' PNe include: (i) the evaporation of primitive material (comets, planetesimals) left over from the formation of the progenitor star (e.g. Liu 2003), which would predict ORL C/O and N/O ratios typical of the unprocessed interstellar medium (ISM) material out of which the star formed; or (ii) that they originated as incompletely mixed material brought to the surface by the third dredge-up and ejected along with the rest of the asymptotic giant branch (AGB) progenitor star's outer envelope during the PN formation phase. In the latter case, the knots' ORL C/O and N/O ratios should show the same nucleosynthetic signatures as the rest of the ejected envelope. Although the postulated H-deficient clumps may not exhibit different kinematics from the bulk of the nebular material, the low inferred electron temperatures of the clumps and the consequent very low thermal broadening means that heavy element ORLs in high-ADF nebulae should exhibit much narrower linewidths than do the strong forbidden lines. For example, a C II λ4267 line originating from 1000-K material should have a FWHM of 2 km s^{-1} if thermal broadening dominates, i.e. if velocity broadening of the line is minimal, as when the emission comes from the edge of the nebula, where material is moving in the plane of the sky, or comes from well-separated approaching and receding velocity components, e.g. near the centre of the nebula. Thus, observations of suitably chosen nebular subregions at a resolving power of 1.5×10^5 may be capable of confirming the presence of the postulated cold plasma clumps.

ACKNOWLEDGMENTS

We thank Daniel Péquignot for illuminating discussions and the referee, Dr S. Torres-Peimbert, for her very careful reading of the manuscript. YGT gratefully acknowledges the award of a Perren Studentship while at University College London and of a Peter Gruber Foundation/International Astronomical Union Fellowship while at the Observatoire de Paris-Meudon.

REFERENCES

Allen C. W., 1973, Astrophysical Quantities. Athlone Press, Univ. London
Allende Prieto C., Lambert D. L., Asplund M., 2001, ApJ, 556, L63
Allende Prieto C., Lambert D. L., Asplund M., 2002, ApJ, 573, L137
Baldwin J. A., Verner E. M., Verner D. A., Ferland G. J., Martin P. G., Korista K. T., Rubin R. H., 2000, ApJS, 129, 229
Barker T., 1991, ApJ, 371, 217
Barlow M. J., 1987, MNRAS, 227, 161
Borkowski K. J., Harrington J. P., Tsvetanov Z., Clegg R. E. S., 1993, ApJ, 415, L47
Cahn J. H., Kaler J. B., Stanghellini L., 1992, A&AS, 94, 399 (CKS92)
Davey A. R., Storey P. J., Kisielius R., 2000, A&AS, 142, 85
Dopita M. A., Ford H. C., Bohlin R., Evans I. N., Meatheringham S. J., 1993, ApJ, 418, 804
Dopita M. A. et al., 1996, ApJ, 460, 320
Ercolano B., Barlow M. J., Storey P. J., Liu X.-W., Rauch T., Werner K., 2003, MNRAS, 344, 1145
Escalante V., Victor G. A., 1990, ApJS, 73, 513
Garnett D. R., Dinerstein H. L., 2001a, in Lee W. H., Torres-Peimbert S., eds, Rev. Mex. Astron. Astrofis. Ser. Conf., Vol. 10, The Seventh Texas–Mexico Conference on Astrophysics: Flows, Blows, and Glows. Inst. de Astron., Univ. Nacional Autonoma de México, México, p. 13
Garnett D. R., Dinerstein H. L., 2001b, ApJ, 558, 145
Grevesse N., Noels A., Sauval A. J., 1996, inHolt. S. S., Sonneborn G., eds, ASP Conf. Ser. Vol. 99, Cosmic Abundances. Astron. Soc. Pac., San Francisco, p. 117
Harrington J. P., Feibelman W. A., 1984, ApJ, 277, 716
Hyung S., Aller L. H., Feibelman W. A., 1999, ApJ, 514, 878
Kaler J. B., 1981, ApJ, 249, 201
Kaler J. B., 1986, ApJ, 308, 322
Kingsburgh R. L., Barlow M. J., 1994, MNRAS, 271, 257 (KB94)
Kuhn H. G., 1969, Atomic Spectra, 2nd edn. Longman, London
Liu X.-W., 1998, MNRAS, 295, 699
Liu X.-W., 2003, inKwok S., Dopita M. A., Sutherland R., eds, Proc. IAU Symp. 209, Planetary Nebulae: Their Evolution and Role in the Universe. Astron. Soc. Pac., San Francisco, p. 339
Liu X.-W., Danziger I. J., 1993a, MNRAS, 261, 465
Liu X.-W., Danziger I. J., 1993b, MNRAS, 263, 256 (LD93b)
Liu X.-W., Storey P. J., Barlow M. J., Clegg R. E. S., 1995, MNRAS, 272, 369 (LSBC)
Liu X.-W., Storey P. J., Barlow M. J., Danziger I. J., Cohen M., Bryce M., 2000, MNRAS, 312, 585
Liu X.-W. et al., 2001a, MNRAS, 323, 343
Liu X.-W., Luo S.-G., Barlow M. J., Danziger I. J., Storey P. J., 2001b, MNRAS, 327, 141
Meaburn J., Walsh J. R., Clegg R. E. S., Walton N. A., Taylor D., Berry D. S., 1992, MNRAS, 255, 177
Meatheringham S. J., Dopita M. A., Morgan D. H., 1988, ApJ, 329, 166
Meatheringham S. J., Dopita M. A., 1991, ApJS, 75, 407
Nussbaumer H., Storey P. J., 1984, A&AS, 56, 293
O'Dell C. R., Henney W. J., Burkert A., 2000, AJ, 119, 2910
O'Dell C. R., Balick B., Hajian A. R., Henney W. J., Burkert A., 2002, AJ, 123, 3329
Peimbert M., 1967, ApJ, 150, 825
Peimbert M., 1971, Bol. Obs. Tonantzintla y Tacubaya, 6, 29
Peimbert M., Storey P. J., Torres-Peimbert S., 1993, ApJ, 414, 626
Peimbert M., Luridiana V., Torres-Peimbert A., 1995, Rev. Mex. Astron. Astrofis., 31, 147
Peimbert M., Peimbert A., Ruiz M. T., Esteban C., 2004, ApJS, 150, 431
Péquignot D., Petitjean P., Boisson C., 1991, A&A, 251, 680
Péquignot D., Amara M., Liu X.-W., Barlow M. J., Storey P. J., Morisset C., Torres-Peimbert S., Peimbert M., 2002, in Henney W. J., Franco J., Martos M., Peña M., eds, Rev. Mex. Astron. Astrofis. Ser. Conf., Vol. 12, Ionized gaseous nebulae: a conference to celebrate the 60th birthdays of Silvia Torres-Peimbert and Manuel Peimbert. Inst. de Astron., Univ. Nacional Autonoma de México, México, p. 142
Rola C., Stasińska G., 1994, A&A, 281, 199
Rubin R. H., 1989, ApJS, 69, 897
Ruiz M. T., Peimbert M., Peimbert A., Esteban C., 2003, ApJ, 595, 247
Sahu K. C., Desai J. N., 1986, A&A, 161, 357
Shaw R. A., Stanghellini L., Mutchler M., Balick B., Blades J. C., 2001, ApJ, 548, 727
Smits D. P., 1996, MNRAS, 278, 683
Stanghellini L., Shaw R. A., Balick B., Mutchler M., Blades J. C., Villaver E., 2003, ApJ, 596, 997
Storey P. J., 1994, MNRAS, 282, 999
Torres-Peimbert S., Peimbert M., Peña M., 1990, A&A, 233, 540
Tsamis Y. G., 2002, PhD thesis, Univ. London
Tsamis Y. G., Barlow M. J., Liu X.-W., Danziger I. J., Storey P. J., 2003a, MNRAS, 338, 687
Tsamis Y. G., Barlow M. J., Liu X.-W., Danziger I. J., Storey P. J., 2003b, MNRAS, 345, 186 (Paper I)
Tylenda R., 2003, in Kwok S., Dopita M. A., Sutherland R., eds, Proc. IAU Symp. 209, Planetary Nebulae: Their Evolution and Role in the Universe. Astron. Soc. Pac., San Francisco, p. 389
Vassiliadis E., Dopita M. A., Morgan D. H., Bell J. F., 1992, ApJS, 83, 87
Viegas S., Clegg R. E. S., 1994, MNRAS, 271, 993
Wesson R., Liu X.-W., Barlow M. J., 2003, MNRAS, 340, 253

APPENDIX A: CALCULATION OF ELEMENTAL ABUNDANCES FROM RECOMBINATION LINES

In this appendix we discuss the derivation of total C, N and O abundances for our PN sample from ORL ionic abundances. We discuss each PN individually in order to highlight differences in the adopted *icf* scheme.

NGC 3242. The C II λ4267, C III λλ4069, 4187 and λ4650 lines are detected; we adopt $C^{3+}/H^{+} = 2.03 \times 10^{-4}$, as an intensity weighted mean from the λλ4187, 4650 lines only. The unseen C^{+} is corrected for using the KB94 *icf* formula: $icf(C) \equiv 1 + O^{+}/O^{2+} = 1.01$. We calculate the C/H fraction using

$$C/H = icf(C)\,(C^{2+} + C^{2+} + C^{4+})/H^{+}. \qquad (A1)$$

This yields $C/H = 8.45 \times 10^{-4}$; this value is only 2 per cent more than the one found if $C^{4+}/H^{+} = 1.88 \times 10^{-5}$, as derived from C IV λ4658, is not added in. The latter value is an upper limit to the C^{4+}/H^{+} fraction, because λ4658 is blended with [Fe III] λ4658.10.

From an intensity weighted mean of N^{2+}/H^{+} ratios from seven N II lines (see Table 4), we find $N^{2+}/H^{+} = 1.71 \times 10^{-4}$. From the

N III λ4379 line, $N^{3+}/H^+ = 6.85 \times 10^{-5}$. We use the CEL ratio $N^+/N^{2+} = 0.0145$ (see Paper I) to account for the unseen N^+; the error introduced should be negligible, because $N^+/N = 0.008$. Hence, summing three ionic stages, we find $N/H = 2.42 \times 10^{-4}$.

From our extensive O II recombination-line survey, we derive $O^{2+}/H^+ = 6.28 \times 10^{-4}$, from five O II multiplets (Table 6). An ORL O^+/H^+ abundance is not available, so the unseen O^+ is corrected for assuming that the Paper I CEL ratio of $O^+/O^{2+} = 0.0091$ also holds for the ORLs. In view of the minor concentration of O^+ in this object (about 1 per cent), the errors introduced should be negligible. We then employ the KB94 standard *icf* to account for the unseen O^{3+}, $icf(O) \equiv (1 + He^{2+}/He^+)^{2/3} = 1.17$, and calculate the total O/H abundance, using

$$O/H = icf(O)\,(O^+ + O^{2+})/H^+. \qquad (A2)$$

This yields $O/H = 7.41 \times 10^{-4}$. Alternatively, we can adopt $O^{3+}/H^+ = 2.05 \times 10^{-4}$, as derived by LD93a from the O III V8 multiplet at 3265 Å. Hence, summing all three ionic stages we find $O/H = 8.39 \times 10^{-4}$, i.e. 13 per cent larger than yielded by the *icf* method. We adopt this latter value.

NGC 5882. The C II λ4267, C III λλ4069, 4187 and λ4650 lines are detected; we adopt $C^{3+}/H^+ = 5.27 \times 10^{-5}$, as an intensity weighted mean from the λλ4187, 4650 lines only. No C^{4+} is expected to exist, because only 2 per cent of He is in the form of He^{2+}. Using equation (A1) with $icf(C) = 1.03$, we find $C/H = 4.43 \times 10^{-4}$.

From an intensity weighted mean of five N^{2+}/H^+ ratios (Table 4), $N^{2+}/H^+ = 2.24 \times 10^{-4}$ is found. From the N III λ4379 line, $N^{3+}/H^+ = 5.75 \times 10^{-5}$. As for NGC 3242, we use the Paper I CEL ratio to account for the unseen N^+, $N^+/N^{2+} = 0.0278$ in this case; we obtain $N/H = 2.88 \times 10^{-4}$.

From eight O II ORL multiplets we derive $O^{2+}/H^+ = 9.70 \times 10^{-4}$ (Table 6). We account for unseen O^+ as previously, using the Paper I CEL ratio of $O^+/O^{2+} = 0.029$; we have $icf(O) = 1.01$, so equation (A2) yields $O/H = 10.08 \times 10^{-4}$.

NGC 5315. The C II λ4267, C III λ4187 lines are detected; no C^{4+} exists because the He^{2+}/H^+ fraction is negligible. We correct for unseen C^+ using the CEL ratio of $C^+/C^{2+} = 0.08$ (given the small concentration of C^+, about 7 per cent, no significant uncertainty is introduced). Hence, we sum three ionic stages and find $C/H = 7.29 \times 10^{-4}$.

From an intensity weighted mean of four N^{2+}/H^+ ratios (Table 4), $N^{2+}/H^+ = 3.43 \times 10^{-4}$ is found; the N III λ4379 line is not detected. If we assume that $N^+/N^{2+} = 0.163$ and $N^{3+}/N^{2+} = 0.565$ ratios, as given by the CELs (Paper I), are also valid for the ORLs, we can account for both N^+ and N^{3+}, and hence $N/H = 5.93 \times 10^{-4}$. This result may be quite uncertain, because probably the N^{3+}/N^{2+} ratio derived from CELs is not equal to the same ratio as derived from ORLs (cf. the case of NGC 3918 below).

From five O II ORL multiplets, $O^{2+}/H^+ = 8.57 \times 10^{-4}$; although this is a relatively low excitation object, a substantial O^{3+} concentration has however been derived from the λ1401 CEL line (Paper I). If we account for unseen O^+ using the CEL ratio $O^+/O^{2+} = 0.098$, we find $O/H = 9.41 \times 10^{-4}$, ignoring O^{3+}/H^+. However, if we further assume that $O^{3+}/O^{2+} = 0.364$, as given by CELs, also holds for ORLs, then this brings the total ORL abundance up to $O/H = 12.53 \times 10^{-4}$, i.e. 33 per cent higher. We adopt this latter value.

NGC 3918. The C II λ4267, C III λλ4187, 4650 lines are detected; $C^{3+}/H^+ = 1.44 \times 10^{-4}$ is derived, as an intensity weighted mean from the λλ4187, 4650 lines. Using the [Fe III] λ4702 line, we estimate that 67 per cent of the detected λ4658 intensity is due to C^{4+}, i.e. $I(\text{C IV } \lambda4658) = 0.1093$; hence, $C^{4+}/H^+ = 2.62 \times 10^{-5}$. An ORL abundance is not available for C^+, so it was estimated using the Paper I CEL ratio of $C^+/C^{2+} = 0.155$ (given the small ionic concentration of C^+, 9 per cent maximum, the error introduced should be negligible). Adding this to the remaining three ionic stages we find $C/H = 7.50 \times 10^{-4}$. (If instead we correct for C^+ using an $icf(C) = 1.09$, we arrive at a value which is smaller by only 3 per cent.)

From an intensity weighted mean of four N^{2+}/H^+ ratios (Table 4), $N^{2+}/H^+ = 1.42 \times 10^{-4}$ is found; from the N III λ4379 line, $N^{3+}/H^+ = 6.41 \times 10^{-5}$. All of the measured intensity of the λ4606 line is attributed to N IV (no contribution from N II λ4607.2 is expected, because the stronger predicted N II λ4601 line is absent); therefore, $N^{4+}/H^+ = 1.90 \times 10^{-5}$. We account for the missing N^+ using the Paper I CEL ratio of $N^+/N^{2+} = 0.203$; summing all four ionic stages, we have $N/H = 2.56 \times 10^{-4}$. For this PN, we find that, just as is the case for relative ionic fractions of carbon, the CEL N^{3+}/N^{2+} ratio (= 1.22) is not equal to the ORL N^{3+}/N^{2+} ratio (= 0.45).

We have derived O^{2+}/H^+ and O^{4+}/H^+ abundances from five O II multiplets (Table 6) and the O IV λ4632 line (Table 7), respectively: $O^{2+}/H^+ = 5.36 \times 10^{-4}$ and $O^{4+}/H^+ = 4.74 \times 10^{-5}$. We account for unseen O^+ and O^{3+}, using the Paper I CEL ratios of $O^+/O^{2+} = 0.086$ and $O^{3+}/O^{2+} = 1.21$; hence, summing all four ionic stages we have $O/H = 12.32 \times 10^{-4}$.

NGC 2022. The C II λ4267, C III λλ4069, 4187 and λ4650 lines as well as the C IV λ4658 line are detected; $C^{3+}/H^+ = 3.10 \times 10^{-4}$ is the intensity weighted mean from the λλ4187, 4650 lines only. We attribute all of the λ4658 intensity to C IV, because other [Fe III] lines are not present; furthermore, this is a very high-excitation object ($He^{2+}/He = 0.88$) and we expect a substantial concentration of C^{4+}; we find $C^{4+}/H^+ = 2.62 \times 10^{-4}$. Using $icf(C) = 1.02$, to correct for unseen C^+ and summing the three higher ionic stages, we obtain $C/H = 14.84 \times 10^{-4}$.

We derive $N^{2+}/H^+ = 4.38 \times 10^{-4}$ from an intensity-weighted mean of three N^{2+}/H^+ ratios (Table 4); from N III λ4379, $N^{3+}/H^+ = 2.08 \times 10^{-4}$ and from N IV λ4606, $N^{4+}/H^+ = 3.68 \times 10^{-5}$ (Table 5; as with NGC 3918, no contribution by N II λ4607.2 is found for the λ4606 line). We correct for unseen N^+ using the Paper I CEL ratio $N^+/N^{2+} = 0.013$ and sum a total of four ionic stages to obtain $N/H = 6.88 \times 10^{-4}$.

From four O II multiplets (Table 6) and the O IV λ4632 line (Table 7), respectively, we derive $O^{2+}/H^+ = 13.01 \times 10^{-4}$ and $O^{4+}/H^+ = 1.10 \times 10^{-4}$; we also adopt $O^{3+}/H^+ = 3.62 \times 10^{-4}$, as derived by LD93a from the O III V,8 multiplet at 3265 Å. The unseen O^+ is accounted for using the Paper I CEL ratio of $O^+/O^{2+} = 0.020$; hence, we obtain $O/H = 17.99 \times 10^{-4}$.

NGC 6818. The C II λ4267, C III λλ4069, 4187 and λ4650 and C IV λ4658 lines are detected; $C^{3+}/H^+ = 1.37 \times 10^{-4}$ is the intensity-weighted mean from the λλ4187, 4650 lines only (Table 2). Using exactly the same argument as in the case of NGC 2022, we attribute the λ4658 line to C^{4+} only; we obtain $C^{4+}/H^+ = 4.47 \times 10^{-5}$. If we assume that the ratio $C^+/C^{2+} = 0.129$ derived from the CELs in Paper I is also valid for the ORLs, we deduce a total abundance of $C/H = 7.71 \times 10^{-4}$.

The N II λλ5676, 5679 lines from multiplet V3 are detected; they yield $N^{2+}/H^+ = 4.27 \times 10^{-4}$ (Table 4); from N III λ4379 we find $N^{3+}/H^+ = 8.87 \times 10^{-5}$, while from N IV λ4606 we deduce

$N^{4+}/H^+ = 1.46 \times 10^{-5}$ (Table 5). The unseen N^+ is corrected for using the Paper I CEL ratio $N^+/N^{2+} = 0.241$. Summing a total of four ionic stages, $N/H = 6.33 \times 10^{-4}$ is obtained.

We have derived $O^{2+}/H^+ = 7.33 \times 10^{-4}$ and $O^{4+}/H^+ = 6.41 \times 10^{-5}$ from four O II multiplets (Table 6) and the O IV λ4632 line (Table 7), respectively. We further adopt $O^{3+}/H^+ = 2.37 \times 10^{-4}$, as derived by LD93a from the O III V8 line at 3265 Å. The unseen O^+ is accounted for using the Paper I CEL ratio of $O^+/O^{2+} = 0.090$; hence, $O/H = 11.00 \times 10^{-4}$.

NGC 3132. Only C II λ4267 is detected. If we then use the standard KB94 *icf* to account for unseen C^{3+}, $icf(C) \equiv O/O^{2+} = 1.93$, and calculate the carbon abundance as $C/H = icf(C)\ C^{2+}/H^+$, we then find $C/H = 12.74 \times 10^{-4}$. If instead we assume that the ratio $C^{3+}/C^{2+} = 0.111$ given by the CELs in Paper I is also valid for the ORLs and use it to estimate the ORL C^{3+}/H^+ abundance, we find, $C/H = 13.86 \times 10^{-4}$, i.e. 9 per cent larger. However, from observations of seven PNe it is found that, in general, ORL $C^{3+}/C^{2+} \neq$ CEL C^{3+}/C^{2+}; hence, we adopt the former C/H value.

From three N II ORL lines and the N III λ4379 line we obtain $N^{2+}/H^+ = 3.40 \times 10^{-4}$ and $N^{3+}/H^+ = 2.47 \times 10^{-5}$, respectively. We correct for the unseen N^+ using the Paper I CEL ratio $N^+/N^{2+} = 1.296$ and sum a total of three ionic stages to find $N/H = 8.05 \times 10^{-4}$.

From the O II V1 and V10 multiplets (Table 6) we have derived $O^{2+}/H^+ = 8.15 \times 10^{-4}$. We account for unseen O^{3+} using an $icf(O) = 1.02$ from equation (A2); we account for unseen O^+ using the Paper I CEL ratio of $O^+/O^{2+} = 0.894$, hence $O/H = 15.74 \times 10^{-4}$. The concentration of O^+ in this PN is about 46 per cent and it may be that some uncertainty has been introduced by assuming that the CEL O^+/O^{2+} ratio equals the ORL O^+/O^{2+} ratio.

NGC 2440. The C II λ4267, C III λλ4187, 4650 and C IV λ4658 lines are detected; we attribute the λ4658 intensity solely to C^{4+}, and thus $C^{3+}/H^+ = 1.66 \times 10^{-4}$ and $C^{4+}/H^+ = 1.82 \times 10^{-4}$ (Table 2). Using the KB94 $icf(C) \equiv 1 + O^+/O^{2+} = 1.28$ to account for unseen C^+ and summing the three higher ionic stages, we find $C/H = 10.21 \times 10^{-4}$.

Four N II lines are detected (Table 4). Their intensity weighted mean yields $N^{2+}/H^+ = 4.77 \times 10^{-4}$; from N III λ4379 we find $N^{3+}/H^+ = 1.43 \times 10^{-4}$. Both N IV λλ4606, 4707 lines are detected, yielding a mean $N^{4+}/H^+ = 1.70 \times 10^{-4}$. No N^+ abundance is available either from ORLs or CELs (our wavelength coverage did not include the [N II] lines). Thus, we adopt the KB94 CEL ratio of $N^+/N^{2+} = 0.475$, and use it to correct for the unseen N^+; summing four ionic stages we obtain $N/H = 10.17 \times 10^{-4}$.

From four O II multiplets and the O IV λ4632 line, respectively, we derive $O^{2+}/H^+ = 5.23 \times 10^{-4}$ and $O^{4+}/H^+ = 1.01 \times 10^{-4}$. We further adopt $O^{3+}/H^+ = 2.56 \times 10^{-4}$, as derived by Liu & Danziger (1993a) from the O III V8 line at 3265 Å, together with the CEL ratio $O^+/O^{2+} = 0.285$ from the same authors (as reported for their position angle of 270^o slit). We assume that this ratio is also valid for ORLs, and hence derive $O/H = 10.29 \times 10^{-4}$.

NGC 6302. Only C II λ4267 is reliably detected; using the same *icf* scheme as for NGC 3132, yields $icf(C) = 2.72$. From equation (A1) we obtain $C/H = 5.45 \times 10^{-4}$.

Three N II lines are detected (Table 4). Their intensity weighted mean yields $N^{2+}/H^+ = 5.64 \times 10^{-4}$; N III λ4379 yields $N^{3+}/H^+ = 8.07 \times 10^{-4}$; N IV λ4606 yields $N^{4+}/H^+ = 2.28 \times 10^{-4}$ (no contribution is expected from N II λ4607). N^+ is accounted for using the CEL ratio $N^+/N^{2+} = 0.435$; summing four ionic stages we find $N/H = 11.18 \times 10^{-4}$.

We obtain $O^{2+}/H^+ = 3.28 \times 10^{-4}$ from the O II V1 multiplet; $O^{4+}/H^+ = 7.84 \times 10^{-5}$ is derived from O IV λ4632. We assume that the Paper I CEL ratios of $O^+/O^{2+} = 0.092$ and $O^{3+}/O^{2+} = 0.895$ are valid for ORLs as well, and deduce $O/H = 7.30 \times 10^{-4}$.

IC 4406. C II λ4267, C III λλ4187, 4650 are detected (Table 2); the He^{2+} concentration is only 6 per cent, so it is assumed that the C^{4+}/H^+ abundance is negligible. Using equation (A1), with $icf(C) = 1.31$ to account for unseen C^+, we find $C/H = 11.27 \times 10^{-4}$ (Table 2).

From the sole detected N II λ4630 line, $N^{2+}/H^+ = 1.90 \times 10^{-4}$; from N III λ4379, $N^{3+}/H^+ = 7.31 \times 10^{-5}$. N^+ is accounted for using the CEL ratio $N^+/N^{2+} = 0.536$; summing three ionic stages we find $N/H = 3.65 \times 10^{-4}$ (Table 5).

We obtain $O^{2+}/H^+ = 7.06 \times 10^{-4}$ and use an $icf(O) = 1.04$ to correct for unseen O^{3+}; the missing O^+ is corrected for using the Paper I CEL ratio of $O^+/O^{2+} = 0.471$ (some error may be introduced because in this object, the O^+ concentration is about 31 per cent of all oxygen). Hence, from equation (A2) we obtain $O/H = 10.80 \times 10^{-4}$.

IC 4191. C II λ4267, C III λλ4187, 4650 are detected (Table 2); $C^{3+}/H^+ = 1.07 \times 10^{-4}$ is found. No significant C^{4+} is present. Using equation (A1) with $icf(C) = 1.04$ to account for unseen C^+, we find $C/H = 6.48 \times 10^{-4}$.

Six N II lines have been detected (Table 4); an intensity weighted mean yields $N^{2+}/H^+ = 5.00 \times 10^{-4}$; from N III λ4379, we derive $N^{3+}/H^+ = 1.15 \times 10^{-4}$ (Table 5). N^+ is accounted for using the Paper I CEL ratio of $N^+/N^{2+} = 0.393$, where $N^{2+}/H^+ = 2.45 \times 10^{-5}$ from the [N III] 57-μm line, as given by Liu et al. (2001a) and N^+/H^+ from our optical observations. Hence, summing three ionic stages we obtain $N/H = 8.12 \times 10^{-4}$.

We derive $O^{2+}/H^+ = 12.92 \times 10^{-4}$ from four O II multiplets (Table 6) and use an $icf(O) = 1.07$ to correct for unseen O^{3+}. The missing O^+ is corrected for using the CEL ratio of $O^+/O^{2+} = 0.041$ (the error introduced in this case should be negligible, because the O^+ concentration in this PN is only about 4 per cent). Hence, we deduce $O/H = 14.39 \times 10^{-4}$.

My Cn 18. Only C II λ4267 is seen; no significant amounts of C^{3+} or C^{4+} are expected. Using equation (A1) with $icf(C) = 1.59$ to account for unseen C^+, we find $C/H = 6.04 \times 10^{-4}$.

Three N II lines of multiplet V5 have been detected (Table 4); from an intensity weighted mean $N^{2+}/H^+ = 20.35 \times 10^{-4}$ is derived. Apart from optical CELs no other information on N exists for this PN and the standard KB94 *icf* scheme cannot account for unseen ionization stages. Therefore, as a lower limit we adopt $N/H \geqslant 20.35 \times 10^{-4}$.

We derive $O^{2+}/H^+ = 6.43 \times 10^{-4}$ from the O II V1 λλ4649, 4650 lines emitted by this low-excitation nebula; unseen O^+ is corrected for using the Paper I CEL ratio of $O^+/O^{2+} = 0.59$ (O^+ represents a significant amount of the total oxygen, about 37 per cent). The resulting $O/H = 10.24 \times 10^{-4}$ may be somewhat uncertain.

SMC N87. C II λ4267, C III λλ4187, 4650 are detected (Table 3); $C^{3+}/H^+ = 6.75 \times 10^{-5}$ is found. No C^{4+} is present; using equation (A1) with $icf(C) = 1.02$ to account for the unseen C^+ only, we find $C/H = 7.55 \times 10^{-4}$. If instead we assume that the ratio of

$C^+/C^{2+} = 0.095$ derived from CELs in Paper I is also valid for the ORLs, we arrive at the same total C/H value.

We derive $O^{2+}/H^+ = 2.95 \times 10^{-4}$ from the O II V1 multiplet (Table 3). Unseen O^+ is corrected for using the Paper I CEL ratio $O^+/O^{2+} = 0.018$ (this is a medium excitation PN and the concentration of O^+ is only about 2 per cent). We obtain $O/H = 3.00 \times 10^{-4}$.

LMC N66. This is a highly ionized nebula reminiscent of the galactic type I PN NGC 6302. No ORLs of carbon are detected, consistent with the carbon-poor, nitrogen-rich nature deduced for this nebula from the CEL analysis of Paper I, and hence no ORL C/H value is available for this object.

From an intensity weighted mean of O II λλ4649, 4650 (Table 3), we derive $O^{2+}/H^+ = 8.53 \times 10^{-4}$. We adopt $icf(O) = 3.77$ (from equation A7 of KB94 coupled with our Paper I CEL ionic nitrogen abundances for this PN). We account for unseen O^+ using the CEL ratio $O^+/O^{2+} = 0.076$ and obtain $O/H = 3.46 \times 10^{-3}$.

LMC N141. C II λ4267, C III λλ4187, 4650 are detected (Table 3); $C^{3+}/H^+ = 5.82 \times 10^{-5}$ is found. No C^{4+} is present; using equation (A1), with $icf(C) = 1.02$ to account for the unseen C^+, we find $C/H = 7.54 \times 10^{-4}$. If instead we assume that the ratio $C^+/C^{2+} = 0.203$ derived from the CELs in Paper I is also valid for the ORLs, we obtain $C/H = 8.75 \times 10^{-4}$. In view of the error this may introduce, we adopt the former value.

We derive $O^{2+}/H^+ = 4.96 \times 10^{-4}$ from the O II V1 and V10 multiplets. Unseen O^+ is corrected for using the Paper I CEL ratio of $O^+/O^{2+} = 0.023$, and we obtain $O/H = 5.08 \times 10^{-4}$.

Nitrogen ORLs have not been detected from either SMC N87, LMC N66 or LMC N141, and hence no inference can be made about their N abundances from ORLs.

APPENDIX B: COMPARISON OF OBSERVED AND PREDICTED INTENSITIES OF O II ORLS

In Table B1 we present a comparison of the dereddened O II line intensities detected from all nebulae, against the predicted intensities from recombination theory. The comparison is relative to the strongest expected line within each multiplet for the 3–3 transitions, while for the collection of 3d–4f transitions it is relative to the strongest expected 3d–4f line at 4089.3 Å. The figures in brackets are the estimated absolute errors in the values, arising from the line profile fitting method only, and do not include any possible systematic errors (for instance, those arising from the calibration process or the corrections for atmospheric and interstellar extinction). In the case of some of the 4f–3d lines, additional, weaker, lines from the same multiplet contribute, as listed in table 4(a) of LSBC. The I_{obs} values listed for some of the 4f–3d lines in Table B1 therefore include contributions from weaker components of the multiplet. However, the contributions from such blending lines were corrected for using the theoretical branching ratios listed in table 4(a) of LSBC in order to arrive at the I_{obs}/I_{pred} values in the final column of Table B1, which refer to the listed multiplet component alone.

Table B1. Comparison of observed and predicted relative intensities of O II lines.

λ_0(Å)	Mult.	g_l–g_u	I_{obs}	I_{obs}/I_{pred}
		NGC 3242		
3s–3p				
4638.86	V1	2–4	0.78[0.08]	3.8[0.4]
4641.81	V1	4–6	1.00[0.07]	1.9[0.1]
4649.13	V1	6–8	1.00	1.0
4650.84	V1	2–2	0.48[0.05]	2.3[0.2]
4661.63	V1	4–4	0.40[0.04]	1.5[0.1]
4673.73	V1	4–2	0.14[0.01]	3.4[0.3]
4676.24	V1	6–6	0.27[0.02]	1.2[0.1]
4317.14	V2	2–4	0.64[0.08]	1.5[0.2]
4319.63	V2	4–6	0.32[0.06]	0.7[0.1]
4325.76	V2	2–2	0.44[0.07]	5.5[0.9]
4345.56	V2	4–2	1.24[0.25]	3.0[0.6]
4349.43	V2	6–6	1.00	1.0
4366.89	V2	6–4	1.28[0.21]	2.8[0.5]
4414.90	V5	4–6	1.00	1.0
4416.97	V5	2–4	0.95[0.15]	1.7[0.3]
4452.37	V5	4–4	0.51[0.17]	4.6[1.5]
3p–3d				
4069.89	V10	4–6	1.10[0.22]	1.5[0.4]
4072.16	V10	6–8	1.29[0.21]	1.9[0.3]
4075.86	V10	8–10	1.00	1.0
4078.84	V10	4–4	0.13[0.03]	1.2[0.3]
4085.11	V10	6–6	0.21[0.04]	1.6[0.3]
4092.93	V10	8–8	0.14[0.04]	1.6[0.4]
4121.46	V19	2–2	0.90[0.59]	2.5[1.6]
4129.32	V19	4–2	1.70[0.24]	21.[3.0]
4132.80	V19	2–4	0.69[0.15]	1.0[0.2]
4153.30	V19	4–6	1.00	1.0
4156.53	V19	6–4	1.23[0.20]	7.7[1.3]
4169.22	V19	6–6	0.41[0.07]	1.2[0.2]
3d–4f				
4083.90	V48b	6–8	0.19[0.03]	0.7[0.1]
4087.15	V48c	4–6	0.18[0.03]	0.7[0.1]
4089.29	V48a	10–12	1.00	1.0
4275.55	V67a	8–10	0.28[0.05]	0.4[0.1]
4276.75	V67b	6–8	0.25[0.04]	1.0[0.1]
4277.43	V67c	2–4	0.15[0.02]	0.7[0.1]
4282.96	V67c	4–6	0.08[0.01]	0.5[0.1]
4283.73	V67c	4–4	0.09[0.01]	0.9[0.1]
4285.69	V78b	6–8	0.11[0.01]	0.6[0.1]
4288.82	V53c	2–4	0.05[0.02]	0.5[0.2]
4291.25	V55	6–8	0.15[0.04]	0.9[0.2]
4292.21	V78c	6–6	0.08[0.03]	0.9[0.3]
4294.78	V53b	4–6	0.28[0.03]	1.0[0.1]
4303.83	V53a	6–8	0.52[0.09]	1.1[0.2]
4307.23	V53b	2–4	0.08[0.02]	0.7[0.2]
4313.44	V78a	8–10	0.08[0.02]	0.7[0.2]
4353.59	V76c	6–8	0.09[0.02]	0.9[0.2]
4357.25	V63a	6–8	0.16[0.02]	2.7[0.3]
4466.42	V86b	4–6	0.23[0.06]	2.3[0.6]
4477.90	V88	4–6	0.13[0.03]	1.4[0.3]
4489.49	V86b	2–4	0.05[0.02]	0.7[0.3]
4491.23	V86a	4–6	0.21[0.02]	1.5[0.1]
4609.44	V92a	6–8	0.20[0.23]	0.5[0.4]
4669.27	V89b	4–6	0.11[0.02]	2.8[0.5]

Table B1 – *continued*

λ_0(Å)	Mult.	g_l–g_u	I_{obs}	I_{obs}/I_{pred}
		NGC 5882		
3s–3p				
4638.86	V1	2–4	0.47[0.05]	2.2[0.1]
4641.81	V1	4–6	0.70[0.05]	1.3[0.1]
4649.13	V1	6–8	1.00	1.0
4650.84	V1	2–2	0.33[0.02]	1.6[0.1]
4661.63	V1	4–4	0.33[0.02]	1.2[0.1]
4673.73	V1	4–2	0.05[0.01]	1.2[0.3]
4676.24	V1	6–6	0.25[0.02]	1.1[0.1]
4317.14	V2	2–4	0.70[0.20]	1.8[0.5]
4319.63	V2	4–6	0.37[0.13]	0.9[0.3]
4345.56	V2	4–2	1.21[0.50]	3.0[1.3]
4349.43	V2	6–6	1.00	1.0
4414.90	V5	4–6	1.00	1.0
4416.97	V5	2–4	0.91[0.22]	1.6[0.4]
3p–3d				
4069.89	V10	4–6	0.49[0.16]	0.7[0.2]
4072.16	V10	6–8	0.87[0.14]	1.3[0.2]
4075.86	V10	8–10	1.00	1.0
4085.11	V10	6–6	0.11[0.04]	0.9[0.3]
4092.93	V10	8–8	0.08[0.02]	0.9[0.2]
4121.46	V19	2–2	0.30[0.23]	0.8[0.6]
4132.80	V19	2–4	0.56[0.08]	0.8[0.1]
4153.30	V19	4–6	1.00	1.0
4156.53	V19	6–4	0.76[0.05]	4.8[0.3]
4169.22	V19	6–6	0.29[0.06]	0.9[0.2]
4110.78	V20	4–2	0.39[0.07]	1.4[0.3]
4119.22	V20	6–8	1.00	1.0
4890.86	V28	4–2	0.13[0.07]	0.5[0.3]
4906.83	V28	4–4	0.55[0.17]	0.9[0.3]
4924.53	V28	4–6	1.00	1.0
3d–4f				
4083.90	V48b	6–8	0.15[0.05]	0.5[0.2]
4087.15	V48c	4–6	0.25[0.04]	0.9[0.1]
4089.29	V48a	10–12	1.00	1.0
4275.55	V67a	8–10	0.40[0.07]	0.6[0.1]
4276.75	V67b	6–8	0.16[0.07]	0.7[0.3]
4277.43	V67c	2–4	0.18[0.04]	0.8[0.2]
4291.25	V55	6–8	0.15[0.03]	0.9[0.2]
4292.21	V18c	6–6	0.05[0.03]	0.6[0.4]
4294.78	V53b	4–6	0.11[0.02]	0.4[0.1]
4303.83	V53a	6–8	0.39[0.04]	0.8[0.1]
4353.59	V76c	6–8	0.10[0.01]	1.0[0.1]
4366.53	V75a	6–8	0.42[0.05]	0.6[0.1]
4466.42	V86b	4–6	0.21[0.05]	2.3[0.6]
4491.23	V86a	4–6	0.14[0.03]	1.0[0.2]
4609.44	V92a	6–8	0.42[0.08]	1.0[0.2]

Table B1 – *continued*

λ_0(Å)	Mult.	g_l–g_u	I_{obs}	I_{obs}/I_{pred}
		NGC 5315		
3s–3p				
4638.86	V1	2–4	0.49[0.04]	2.3[0.2]
4641.81	V1	4–6	0.66[0.05]	1.3[0.1]
4649.13	V1	6–8	1.00	1.0
4650.84	V1	2–2	0.25[0.03]	1.2[0.1]
4661.63	V1	4–4	0.25[0.02]	0.9[0.1]
4673.73	V1	4–2	0.04[0.01]	1.0[0.3]
4676.24	V1	6–6	0.22[0.01]	1.0[0.1]
4317.14	V2	2–4	1.00	1.0
4319.63	V2	4–6	0.71[0.10]	0.7[0.1]
4325.76	V2	2–2	0.28[0.04]	1.5[0.2]
4345.56	V2	4–2	0.92[0.20]	1.0[0.3]
4349.43	V2	6–6	1.07[0.20]	0.5[0.1]
4366.89	V2	6–4	0.85[0.40]	0.8[0.3]
4414.90	V5	4–6	1.00	1.0
4416.97	V5	2–4	0.86[0.50]	1.5[0.9]
4452.37	V5	4–4	0.20[0.11]	1.8[1.0]
3p–3d				
4069.62	V10	4–6	3.02[2.2]	4.1[3.0]
4072.16	V10	6–8	1.33[1.0]	1.9[1.4]
4075.86	V10	8–10	1.00	1.0
4085.11	V10	6–6	0.31[0.21]	2.4[1.6]
3d–4f				
4083.90	V48b	6–8	0.27[0.05]	0.9[0.2]
4087.15	V48c	4–6	0.35[0.04]	1.3[0.2]
4089.29	V48a	10–12	1.00	1.0
4275.55	V67a	8–10	1.17[0.20]	1.0[0.2]
4303.82	V53a	6–8	0.37[0.06]	0.8[0.1]
4609.44	V92a	6–8	0.53[0.04]	1.2[0.1]
		NGC 3918		
3s–3p				
4638.86	V1	2–4	1.04[0.23]	5.0[1.1]
4641.81	V1	4–6	1.03[0.40]	1.9[0.7]
4649.13	V1	6–8	1.00	1.0
4650.84	V1	2–2	0.26[0.07]	1.3[0.4]
4661.63	V1	4–4	0.35[0.04]	1.3[0.2]
4673.73	V1	4–2	0.15[0.03]	3.5[0.8]
4676.24	V1	6–6	0.31[0.02]	1.4[0.1]
4317.14	V2	2–4	1.00	1.0
4319.63	V2	4–6	0.41	0.4
4325.76	V2	2–2	0.34	1.9
4349.43	V2	6–6	1.53	0.7
4414.90	V5	4–6	1.00	1.0
4416.97	V5	2–4	0.56	1.0
4452.37	V5	4–4	1.26	11.
3p–3d				
4069.62	V10	4–6	8.11[4.1]	11[5.6]
4072.16	V10	6–8	3.62[1.8]	5.3[2.6]
4075.86	V10	8–10	1.00	1.0
4085.11	V10	6–6	0.30[0.22]	2.3[1.7]
4121.46	V19	2–2	3.54	9.8
4132.80	V19	2–4	0.69	1.0
4153.30	V19	4–6	1.00	1.0
4156.53	V19	6–4	1.42	8.9
4169.22	V19	6–6	0.18	0.5

Table B1 – *continued*

λ_0(Å)	Mult.	g_l–g_u	I_{obs}	I_{obs}/I_{pred}
		NGC 3918		
3d–4f				
4083.90	V48b	6–8	0.50[0.18]	1.7[0.6]
4087.15	V48c	4–6	0.43[0.17]	1.6[0.6]
4089.29	V48a	10–12	1.00	1.0
4275.55	V67a	8–10	1.15	0.9
4291.25	V55	6–8	0.44	1.7
4294.78	V53b	4–6	0.45	1.6
4303.83	V53a	6–8	0.50	1.1
4466.42	V86b	4–6	0.43	4.3
4610.20	V92c	4–6	0.67	1.2
4669.27	V89b	4–6	0.22	5.5
		NGC 2022		
3s–3p				
4638.86	V1	2–4	0.32[0.11]	1.5[0.5]
4641.81	V1	4–6	1.10[0.16]	2.1[0.3]
4649.13	V1	6–8	1.00	1.0
4650.84	V1	2–2	0.15[0.21]	0.7[1.0]
4661.63	V1	4–4	0.33[0.06]	1.2[0.2]
4676.24	V1	6–6	0.23[0.08]	1.0[0.4]
3p–3d				
4072.16	V10	6–8	1.07[0.17]	1.6[0.3]
4075.86	V10	8–10	1.00	1.0
3d–4f				
4089.29	V48a	10–12	1.00	1.0
4276.75	V67b	6–8	0.92	1.0
4477.90	V88	4–6	0.54	6.0
4609.44	V92a	6–8	0.29	0.7
		IC 4406		
3s–3p				
4638.86	V1	2–4	0.64[0.11]	3.1[0.5]
4641.81	V1	4–6	0.93[0.12]	1.8[0.2]
4649.13	V1	6–8	1.00	1.0
4650.84	V1	2–2	0.46[0.09]	2.2[0.4]
4661.63	V1	4–4	0.35[0.09]	1.3[0.3]
4676.24	V1	6–6	0.17[0.10]	0.8[0.5]
3p–3d				
4069.62	V10	2–4	1.62[0.60]	2.2[0.8]
4072.16	V10	6–8	1.49[0.51]	2.2[0.8]
4075.86	V10	8–10	1.00	1.0
		NGC 6818		
3s–3p				
4638.86	V1	2–4	1.19[0.30]	5.7[1.4]
4641.81	V1	4–6	2.73[0.41]	5.2[0.8]
4649.13	V1	6–8	1.00	1.0
4650.84	V1	2–2	0.29[0.11]	1.4[0.6]
4661.63	V1	4–4	0.47[0.07]	1.8[0.3]
3p–3d				
4069.78	V10	2–4	0.30[0.26]	0.4[0.4]
4072.16	V10	6–8	0.40[0.14]	0.6[0.2]
4075.86	V10	8–10	1.00	1.0
4085.11	V10	6–6	0.16[0.06]	1.2[0.5]
		NGC 2440		
3s–3p				
4638.86	V1	2–4	2.85[0.56]	14.[2.6]
4641.81	V1	4–6	6.54[0.37]	9.4[0.7]
4649.13	V1	6–8	1.00	1.0
4650.84	V1	2–2	0.20[0.26]	1.0[1.2]
4661.63	V1	4–4	0.35[0.06]	1.3[0.2]
4676.24	V1	6–6	0.71[0.08]	3.2[0.4]
4414.90	V5	4–6	1.00	1.0
4416.97	V5	2–4	0.80[0.22]	1.4[0.4]
4452.37	V5	4–4	1.70[0.37]	15.[3.3]

Table B1 – *continued*

λ_0(Å)	Mult.	g_l–g_u	I_{obs}	I_{obs}/I_{pred}
		IC 4191		
3s–3p				
		Entire nebula		
4638.86	V1	2–4	0.33[0.06]	1.6[0.3]
4641.81	V1	4–6	0.56[0.06]	1.1[0.1]
4649.13	V1	6–8	1.00	1.0
4650.84	V1	2–2	0.27[0.05]	1.3[0.3]
4661.63	V1	4–4	0.27[0.02]	1.0[0.1]
4676.24	V1	6–6	0.22[0.02]	1.0[0.1]
		Fixed slit		
4638.86	V1	2–4	0.34[0.04]	1.6[0.2]
4641.81	V1	4–6	0.28[0.02]	0.5[0.04]
4649.13	V1	6–8	1.00	1.0
4650.84	V1	2–2	0.24[0.03]	1.2[0.2]
4661.63	V1	4–4	0.20[0.03]	0.7[0.1]
4676.24	V1	6–6	0.15[0.02]	0.7[0.1]
4317.14	V2	2–4	1.00	1.0
4319.63	V2	4–6	0.82[0.25]	0.8[0.3]
4345.56	V2	4–2	1.79[0.64]	1.9[0.7]
4349.43	V2	6–6	3.44[1.0]	1.5[0.4]
4366.89	V2	6–4	1.58[0.36]	1.6[0.4]
4414.90	V5	4–6	1.00	1.0
4416.97	V5	2–4	0.81[0.08]	1.4[0.1]
		Entire nebula		
4414.90	V5	4–6	1.00	1.0
4416.97	V5	2–4	0.70[0.19]	1.3[0.4]
4452.37	V5	4–4	0.53[0.14]	4.8[1.3]
3p–3d				
		Entire nebula		
4069.62	V10	4–6	2.45[0.66]	3.3[0.9]
4072.16	V10	6–8	1.27[0.36]	1.8[0.5]
4075.86	V10	8–10	1.00	1.0
4085.11	V10	6–6	0.17[0.09]	1.3[0.7]
		Fixed slit		
4069.62	V10	4–6	1.74[0.38]	2.4[0.5]
4072.16	V10	6–8	1.03[0.25]	1.5[0.4]
4075.86	V10	8–10	1.00	1.0
4085.11	V10	6–6	0.08[0.04]	0.6[0.3]
3d–4f				
		Entire nebula		
4083.90	V48b	6–8	0.28[0.13]	1.0[0.5]
4087.15	V48c	4–6	0.39[0.13]	1.3[0.4]
4089.29	V48a	10–12	1.00	1.0
4275.55	V67a	8–10	1.42[0.28]	1.1[0.2]
4282.96	V67c	4–6	0.40[0.13]	0.9[0.3]
4303.82	V53a	6–8	0.63[0.16]	1.3[0.3]
4609.44	V92a	6–8	0.58[0.10]	1.3[0.2]
		Fixed slit		
4083.90	V48b	6–8	0.34[0.07]	1.2[0.3]
4087.15	V48c	4–6	0.33[0.07]	1.1[0.2]
4089.29	V48a	10–12	1.00	1.0
4275.55	V67a	8–10	1.18[0.18]	1.0[0.2]
4303.82	V53a	6–8	0.33[0.07]	0.7[0.2]
4466.42	V86b	4–6	0.19[0.03]	1.9[0.3]
4609.44	V92a	6–8	0.29[0.08]	0.7[0.1]

Table B1 – *continued*

λ_0(Å)	Mult.	g_l–g_u	I_{obs}	I_{obs}/I_{pred}
		NGC 3132		
3s–3p				
4638.86	V1	2–4	0.53[0.47]	2.6[2.2]
4641.81	V1	4–6	0.88[0.58]	1.7[1.1]
4649.13	V1	6–8	1.00	1.0
4650.84	V1	2–2	0.66[0.38]	3.2[1.8]
4661.63	V1	4–4	0.60[0.34]	2.2[1.3]
4676.24	V1	6–6	0.39[0.23]	1.7[1.1]
3p–3d				
4069.62	V10	2–4	1.14[0.78]	1.5[1.0]
4072.16	V10	6–8	0.41[0.34]	0.6[0.5]
4075.86	V10	8–10	1.00	1.0
4085.11	V10	6–6	0.12[0.03]	0.9[0.2]
		NGC 6302		
3s–3p				
4649.13	V1	6–8	1.00	1.0
4650.84	V1	2–2	0.97	4.7
4661.63	V1	4–4	1.14	5.1
		My Cn 18		
3s–3p				
4649.13	V1	6–8	1.00	1.0
4650.84	V1	2–2	0.37	1.8
		LMC N66		
3s–3p				
4649.13	V1	6–8	1.00	1.0
4650.84	V1	2–2	1.00	4.8

Table B1 – *continued*

λ_0(Å)	Mult.	g_l–g_u	I_{obs}	I_{obs}/I_{pred}
		LMC N141		
3s–3p				
4638.86	V1	2–4	0.20[0.10]	1.0[0.5]
4641.81	V1	4–6	0.95[0.28]	1.8[0.5]
4649.13	V1	6–8	1.00	1.0
4650.84	V1	2–2	0.66[0.41]	3.1[1.9]
4661.63	V1	4–4	0.41[0.14]	1.6[0.6]
4676.24	V1	6–6	0.37[0.09]	1.7[0.4]
3p–3d				
4069.62	V10	2–4	0.74[0.36]	1.0[0.5]
4072.16	V10	6–8	0.49[0.18]	0.7[0.3]
4075.86	V10	8–10	1.00	1.0
		SMC N87		
3s–3p				
4638.86	V1	2–4	1.07[0.17]	5.1[0.8]
4641.81	V1	4–6	1.06[0.26]	2.0[0.4]
4649.13	V1	6–8	1.00	1.0
4650.84	V1	2–2	1.00[0.15]	4.8[0.7]
4661.63	V1	4–4	0.31[0.04]	1.2[0.2]
4676.24	V1	6–6	0.32[0.11]	1.4[0.5]

This paper has been typeset from a TEX/LATEX file prepared by the author.